TEST OF TIME REVERSAL INVARIANCE IN ^{19}Ne BETA DECAY

Contents

TEST OF TIME REVERSAL INVARIANCE IN ^{19}Ne BETA DECAY

Donald Claude Girvin

Department of Physics
and
Lawrence Berkeley Laboratory
University of California
Berkeley, California

March 30, 1972

ABSTRACT

A new experimental upper limit on the "time-reversal" coefficient D is reported for the allowed beta decay $^{19}\mathrm{Ne} \rightarrow \mathrm{F}^{19} e^{+} \nu_e$. The result is given in terms of the relative phase angle between the vector (V) and axial-vector (A) couplings, $\phi_{A,V}(^{19}\mathrm{Ne}) = 180.1 \pm 0.3°$. The V and A couplings are relatively real, implying that T invariance holds in the V-A Theory at zero momentum transfer. The present result does not exclude the possibility of a T violation in the momentum-transfer-dependent weak couplings of the $\Delta S = 0$ hadronic weak current.

The experiment was performed with an atomic beam apparatus in which either of the $m_I = +1/2$ or $m_I = -1/2$ magnetic substates was selected from a beam of $^1S_0$ ground state ^{19}Ne atoms. The polarized beam terminated its flight in a cell (bulb) where the ^{19}Ne atoms remained for approximately 4 seconds without substantial spin relaxation. The

measurement of those delayed coincidences between positrons and the $^{19}F^-$ recoil ions whose momenta are, on the average, perpendicular to the nuclear spin $\vec{I}$ of ^{19}Ne served to measure the "D" coefficient. The nuclear polarization of the ^{19}Ne cointained in the cell was monitored continuously by observation of the positrons emitted parallel and antiparallel to the spin axes.

I. INTRODUCTION

The continuation of an earlier experimental search[1] for a possible violation of time-reversal (T) invariance in the allowed nuclear beta decay of polarized $^{19}\mathrm{Ne} \rightarrow {}^{19}\mathrm{F}^- + e^+ + \nu$ ($\tau_{1/2} = 17.6$ sec, $E_{max} = 2.21$ MeV) has been completed. The new results obtained from this $\Delta S = 0$ weak decay are again consistent with T invariance.

This work was stimulated by the observation of a direct CP violation in the $\Delta S = 1$ decay of $K_2^0 \rightarrow 2\pi$.[2] The magnitude of this CP-violating effect is given in terms of the ratio of CP-violating to CP-conserving amplitudes:

$$\eta^{+-} = \frac{\langle \pi^+\pi^- | H_W | K_L^0 \rangle}{\langle \pi^+\pi^- | H_W | K_S^0 \rangle} = 2.\times 10^{-3} .$$

Subsequent measurements of $K_{\mu 3}$ "charge asymmetries" provide independent evidence of a CP violation: $\delta_e = [\Gamma(K_2^0 \rightarrow \pi^- e^+ \nu) - \Gamma(K_2^0 \rightarrow \pi^+ e^- \nu)] \div [\Gamma(K_2^0 \rightarrow \pi^- e^+ \nu) + \Gamma(K_2^0 \rightarrow \pi^+ e^- \nu)] = 2.2\times 10^{-3}$.[3] Although the parameters essential for a phenomenological description of CP violation in the kaon system have been measured (the phase and magnitude of η_{00} remain ambiguous), the origin of the CP violation remains unclear.

Assuming that CPT invariance is valid, CP violation implies that T invariance also fails. In spite of immense experimental effort, no evidence of direct T violations in (1) strong interactions,[4] (2) the electromagnetic interactions of the hadrons,[5] or (3) weak interactions has been observed.

If the CP violation originates through a first-order weak interaction process, the expected ratio of T-violating to T-conserving amplitudes will be of the order of 10^{-3}. T violations manifest themselves indirectly in first-order weak processes as triple-angular correlations (TAC) between the momenta and spins of the decaying particles. The observation of a T-odd TAC constitutes unambiguous evidence of a T violation, if and only if final-state interactions can be neglected.

The T-odd TAC observed for polarized ^{19}Ne is $D\{\vec{I}\cdot(\vec{p}\times\vec{r})\}$, where $\vec{I}$ is the initial nuclear spin of ^{19}Ne and $\vec{p}$ and $\vec{r}$ are the momenta of the positron and recoil $^{19}F^{-}$ ion. The coefficient D is given by (Sect. II)

$$D = \frac{\frac{2}{\sqrt{3}}|\rho|\sin\phi}{1+\rho^2} \,,$$

where

$$|\rho| = \left| \frac{C_A\langle\sigma\rangle}{C_V\langle 1\rangle} e^{i\phi} \right| = 1.6 \,,^{1}$$

ϕ is the phase between the vector and axial vector coupling constants, and $\langle 1\rangle$ and $\langle\sigma\rangle$ are the Fermi and Gamow-Teller matrix elements. T invariance requires that C_A, C_V be relatively real, i.e., that the relative phase be $\phi = 0$ or π.[6] Thus D must vanish. Alternatively, D will not vanish identically, and ϕ could vary from 180° by as much as $|\pi - \phi| = 0.1°$, if a 10^{-3} T-violating effect exists in first-order weak processes. This follows, since D is proportional to the decay amplitudes.

A beam of neon atoms is polarized in a Stern-Gerlach atomic-beams apparatus, then trapped and held in a cell made of Al, Au, and sapphire, where the ^{19}Ne atoms decay. These decays are observed as delayed coincidences between the positron and the recoil ion. The polarization of the trapped neon gas is maintained by a magnetic field. Maximum sensitivity to D is achieved by observing only those delayed coincidences for which the plane formed by $\vec{p}$ and $\vec{r}$ is, on the average, perpendicular to $\vec{I}$.

The experimental result is

$$D(^{19}\mathrm{Ne}) = 0.001 \pm .003.$$

Using the value of ρ above, the phase angle is

$$\phi(^{19}\mathrm{Ne}) = 180.1 \pm 0.3^\circ \ .$$

The contributions to D from non-T-violating final-state interactions are substantially smaller than the present statistical uncertainty. Our result is consistent with the conservation of T invariance.

The results of this and other experimental tests of T invariance in weak interactions are listed in the table below. The type of T-odd correlation is listed for each decay; the results are quoted in terms of the relative phase ϕ between coupling constants or form factors and the experimental sensitivity to a T-odd amplitude. For the neutron decay, ϕ is the relative phase angle between C_A and C_V. In the $K_{\mu 3}$ decay the transverse polarization of the muon is measured to determine Imξ, where $\xi = f^-/f^+$, and f^+, f^- are form factors for the $\Delta S = +\Delta Q$ and $-\Delta Q$ amplitudes. With Reξ measured elsewhere,[7] $\phi = \tan^{-1} \frac{\mathrm{Im}\xi}{\mathrm{Re}\xi}$. For $\Lambda^0 \to \pi^- p$, the relative phase shifts are measured for the final-state s and p waves, giving $\phi = 9 \pm 5.5°$. Comparing the phase difference $\delta_s - \delta_p = 6.5 \pm 1.5°$[8] in low-energy π-p scattering yields a result consistent with T invariance.

Decay	ΔS	Correlation	Phase ϕ	Sensitivity to T-odd Amp.	Year:Ref.
neon	0	$\sigma_{Ne}\cdot(p\times\nu)$	$180.1 \pm 0.3°$	3×10^{-3}	71:
neutron	0	$\sigma_n\cdot(p\times\nu)$	$178.8 \pm 1.2°$	1×10^{-2}	70:[9]
$K_{\mu3}$	1	$\sigma_\mu\cdot(p_\mu\times p_\pi)$	$0.6 \pm 2.6°$	6×10^{-2}	67:[10]
Λ	1	$p_p\cdot(\sigma_p\times\sigma_\Lambda)$	$<8°$	$\sim10^{-1}$	67:[11]

Our present result, listed above, places a 3×10^{-3} upper limit on the size of a vector-axial vector T violation in ΔS = 0 decays. A factor of 10 improvement on the ^{19}Ne result may reveal a T violation in the V-A theory, yet a null result at the 0.3×10^{-3} level will not necessarily exclude a direct T violation in a ΔS = 1 decay amplitude.

II. THEORY

In this section we will consider the following items as they apply to the present experimental test of T invariance in the mirror decay of ^{19}Ne: (a) the beta decay amplitude and the phase restrictions that T invariance imposes on the individual couplings in the amplitude; (b) the formal expression for the decay rate $d\lambda$ and the T-odd angular correlation term whose coefficient D^{TR} is sensitive to the phase restrictions imposed by T invariance; (c) contributions D^{EM} to the same T-odd angular correlation arising from final-state electromagnetic interactions; and (d) a comparison of the magnitude of D^{EM} to the present experimental uncertainty in D_{exp}, where $D_{exp} = D^{TR} + D^{EM}$ is the experimentally measured quantity. Placement of an upper limit on a possible T violation requires that $D^{EM} <$ error in D_{exp}.

A. Beta Decay Amplitude and Phase Restrictions on Couplings

Assuming a pure V-A coupling, the validity of the CVC hypothesis, and the absence of final-state electromagnetic interactions, the most general form of the beta decay amplitude for the allowed decay of ^{19}Ne is

$$\mathcal{M} = \frac{G}{\sqrt{2}} \cos\theta_C \bar{u}(^{19}F)\left\{V_\mu^{o\dagger} + A_\mu^{o\dagger}\right\}u(^{19}Ne)\ell_\mu \qquad \text{(II-1)}$$

where G $\left(= \frac{10^{-5}}{m_p^2}\right)$ is the universal weak-coupling constant, θ_C (= 15°) is the Cabibbo angle, ℓ_μ is the matrix element of the leptonic current:

$$\ell_\mu = \bar{u}(e)\gamma_\mu(1 + \gamma_5)u(\nu) \ , \qquad \text{(II-2)}$$

and $V_\mu^o + A_\mu^o$ is the $\Delta S = 0$ component of the hadronic weak current given by

$$V^o_\mu + A^o_\mu = f_1\gamma_\mu - if_2\sigma_{\mu\alpha}q_\alpha + g_1\gamma_\mu\gamma_5 - ig_2\sigma_{\mu\alpha}q_\alpha\gamma_5 + g_3q_\mu\gamma_5 . \quad \text{(II-3)}$$

Here $q_\alpha = (p_e + p_\nu)_\alpha = (p_{Ne} - p_F)_\alpha$ is the 4-momentum transfer to the final-state leptons. The f's and g's are the vector and axial-vector form factors, all functions of q^2. Using the standard nomenclature, the vector $[f_1(0)]$ and axial-vector $[g_1(0)]$ terms are the dominant couplings in allowed nuclear beta decay. The weak-magnetism (f_2) term has only a small effect on the expression for the decay rate of ^{19}Ne, while the "second-class"* induced-tensor (g_2) coupling has not yet been experimentally observed. The induced pseudoscaler term g_3 will not be considered, since its contribution to allowed beta decay is negligible.

What restriction does T invariance impose upon the amplitude $\mathcal{M}$ and how can this be observed experimentally in the decay rate $d\lambda$? In the absence of final-state interactions, the hadronic amplitude in Eq. II-1 must have the same T-transformation properties as the leptonic amplitude (ℓ_μ), if T invariance is to hold. Thus T invariance requires that $\eta^V_T = \eta^A_T$, where the etas are defined by

$$TV^o_\mu(x)T^{-1} = -\eta^V_T \, V^o_\mu(x^T)$$

and

$$TA^o_\mu(x)T^{-1} = -\eta^A_T \, V^o_\mu(x^T) \; .$$[13]

These etas are arbitrary phase factors equal to ±1. The condition

---

[*] The Weinberg[12] classification of those terms in V^o_μ (A^o_μ) that are odd (even) under a G transformation is used; G is the combined operation of charge conjugation and isospin rotation.

$\eta_T^V = \eta_T^A$ requires that the form factors f_i and g_i must be relatively real, e.g., $f_i g_j^* = |f_i g_j^*| e^{i\phi_{i,j}}$ where $\phi_{i,j} = 0, \pi$. Without imposing this condition on $\mathcal{M}$, an angular-correlation term proportional to $\mathrm{Im}(f_i g_j^*)$ appears in $d\lambda$. An experimental observation of such a correlation constitutes a violation of T invariance.

The charge-symmetry condition applied to the $\Delta S = 0$ weak current is

$$e^{i\pi T_2} (V_\lambda^o + A_\lambda^o) e^{-i\pi T_2} = \pm (V_\lambda^o + A_\lambda^o)^\dagger \qquad \text{(II-4)}$$

where the operators $e^{\pm i\pi T_2}$ reverse the sign of the third component of isospin and $\vec{T}_2$ is the generator of rotations about the second axis in isospin space. This condition imposes the following restrictions upon the form factors[14]:

$$f_1 = f_1^* , \quad f_2 = f_2^* , \quad g_1 = g_1^* , \quad g_2 = -g_2^* .$$

The form factors must be real except for the induced tensor, which is pure imaginary if charge symmetry is valid. Notice that T invariance imposes the same condition on f_1, f_2, and g_2; only the restriction on the induced tensor term is distinct. The implication of this ambiguity will be considered in Section VI.

B. Formal Expression for dλ and the T-odd Angular Correlation Term

If we ignore nuclear recoil effects, i.e., terms in $\mathcal{M}$ of the order of $mc^2/2M$ where m and M are the masses of the electron and recoil nuclei, then only the f_1 and g_1 terms contribute to the decay rate. Thus, to zero^th order in the nuclear recoil parameter $E_o/2M$,

$$\cong \frac{G\cos\theta_C}{\sqrt{2}} \left[C_V\langle 1\rangle \bar{u}_e \gamma_o (1 + \gamma_5) u_\nu - C_A \langle\vec{\sigma}\rangle \cdot \bar{u}_e \vec{\gamma}(1 + \gamma_5) u_\nu\right] \qquad \text{(II-5)}$$

where form factors or coupling constants are

$$f_1(q^2 \to 0) = C_V = 1 \quad \text{and} \quad g_1(0) = -C_A = -1.2 \ ,$$

the γ's are Dirac matrices, and $\langle 1\rangle$ and $\langle\sigma\rangle$ are the Fermi and Gamow-Teller nuclear matrix elements.

The initial and final nuclear spins in ^{19}Ne decay are equal, i.e., $I_i = I_f = 1/2$. The transition rate $d\lambda$ in the allowed approximation and summed over the final lepton spins is*

$$d\lambda = \left(\frac{1}{2\pi}\right)^5 \frac{(G\cos\theta_C)^2}{\hbar^7 c} F(Z, E) p^2 q^2 \, dp d\Omega_e d\Omega_\nu$$
$$\times \xi\left\{1 + a \frac{\vec{v}}{c} \cdot \hat{q} + \frac{\langle\vec{I}\rangle}{I} \cdot \left[A \frac{\vec{v}}{c} + B\hat{q} + D \frac{\vec{v}}{c} \times \hat{q}\right]\right\} \qquad \text{(II-6)}$$

Here $F(Z, E)$ is the Fermi function; p, v, and E are the magnitude of the momentum, velocity, and energy of the electron (positron); $q = \frac{E_{max} - E}{c}$ and $\hat{q}$ designates the magnitude and direction of the neutrino momentum; and $d\Omega_e$ and $d\Omega_\nu$ are the differential solid angles for the electron and neutrino. The polarization of the initial ensemble of ^{19}Ne nuclei is denoted by $\frac{\langle\vec{I}\rangle}{I}$.

---

* See Refs. 15 and 16. In Ref. 15 the scalar (S), vector (v), axial vector (A), and tensor (T) couplings were included in the calculation of $d\lambda$. The coefficients a, A, etc. given there reduce to the expressions given here upon setting the S and T couplings to zero.

In the absence of final-state interactions the coefficients are

$$\begin{aligned}
\xi &= C_V^2\langle 1\rangle^2 + C_A^2\langle\sigma\rangle^2 \\
\xi a &= C_V^2\langle 1\rangle^2 - \frac{1}{3}C_A^2\langle\sigma\rangle^2 \\
\xi A &= \mp\frac{2}{3}C_A^2\langle\sigma\rangle^2 - \frac{2}{\sqrt{3}}\mathrm{Re}(C_V^*C_A)\langle 1\rangle\langle\sigma\rangle \\
\xi B &= \pm\frac{2}{3}C_A^2\langle\sigma\rangle^2 - \frac{2}{\sqrt{3}}\mathrm{Re}(C_V^*C_A)\langle 1\rangle\langle\sigma\rangle \\
\xi D^{TR} &= \mp\frac{2}{\sqrt{3}}\mathrm{Im}(C_V^*C_A)\langle 1\rangle\langle\sigma\rangle\ .
\end{aligned}$$

The upper (lower) sign refers to electron (positron) emission. These coefficients can be rewritten in terms of ρ, where

$$\rho = \frac{C_A}{C_V}\frac{\langle\sigma\rangle}{\langle 1\rangle} = \left|\frac{C_A}{C_V}\right|\cdot\left|\frac{\langle\sigma\rangle}{\langle 1\rangle}\right|e^{i(\theta + \phi_{A,V})}\ .$$

θ is the relative phase between the nuclear matrix elements, and $\phi_{A,V}$ the relative phase of the vector and axial-vector couplings. In particular, the D coefficient for the T-odd angular-correlation term is

$$D^{TR}({}^{19}\mathrm{Ne}) = +\frac{2}{\sqrt{3}}\frac{|\rho|}{1+\rho^2}\sin(\theta + \phi_{A,V})\ . \qquad \text{(II-8)}$$

With the phase convention for the nuclear wave functions of ^{19}Ne giving $\theta({}^{19}\mathrm{Ne}) = \pi$,[17] T conservation ($\phi_{A,V} = 0$) requires that D^{TR} vanish.

Using the value $|\rho({}^{19}\mathrm{Ne})| = 1.6$,[1,29] we have $D^{TR}({}^{19}\mathrm{Ne}) = 0.518\ \sin\phi_{A,V}$. The superscript "TR" designates that part of the "total" D coefficient which is sensitive to a T violation. Final-state electromagnetic interactions can introduce a correlation term $D^{EM}\hat{I}\cdot(\vec{v}\times\hat{q})$ in $d\lambda$. The coefficient D^{EM} is proportional to $\mathrm{Re}(C_A^*C_V)$ and therefore has no relation to T invariance. Thus the distinction between the two contributions to the total quantity D_{exp}.

The effect of weak magnetism and second-class induced tensor couplings upon the angular-correlation coefficients in $d\lambda$ can be examined only when first-order terms in the nuclear-recoil parameter $E/2M$ ($\sim 10^{-4}$ for ^{19}Ne) are included in the transition amplitude $\mathcal{M}$. With the present experimental uncertainty in D_{exp}, it is important to evaluate the f_2 and possible g_2 contributions to D^{TR}. Including these terms in the transition amplitude, Holstein[18] obtained

$$D^{TR} = \mp\frac{1}{\xi}\left\{\frac{1}{\sqrt{3}}\left[2\ \mathrm{Im}(C_V^* C_A)\langle 1\rangle\langle\sigma\rangle - \mathrm{Im}\ a^*(c \pm d \pm b)\frac{E_0}{M}\right.\right.$$
$$- \mathrm{Im}\ a^*\left((c \pm d \mp b)\frac{E_0}{M} + 2(3c \pm b)\frac{E}{M}\right)$$
$$\left.\left. + \frac{2}{3}\,\mathrm{Im}\ c^*\left((d + b)\frac{E_0}{2M} - d\,\frac{E}{M}\right)\right]\right\} \quad . \qquad \text{(II-10)}$$

The upper (lower) signs refer to electron (positron) emission, where ξ is given above, E_0 is the electron (positron) rest energy, M the mass of the recoil nucleus, and <u>a</u> and <u>c</u> are $a = C_V\langle 1\rangle$, $c = C_A\langle\sigma\rangle$. The <u>b</u> and <u>d</u> terms arise from the weak-magnetism and induced-tensor couplings.

The form factor $f_2(0)$ is contained in <u>b</u>. f_2 is evaluated in terms of the parent and daughter nuclear magnetic moments, according to the conserved vector current (CVC) hypothesis. Defining μ as the difference in nuclear magnetic moments, $\mu = \mu(^{19}\mathrm{Ne}) - \mu(^{19}\mathrm{F})$ in units of nuclear magnetons, we have

$$b = \sqrt{3}\,\frac{M}{m_p}\,(\langle 1\rangle\cdot\mu)e^{i\phi_W} .$$

The phase of f_2 is denoted by ϕ_W, and m_p is the nucleon mass.

Defining μ_2 as a parameter representing the magnitude of the induced-tensor coupling, we have

$$d = \mu_2 \left(\frac{\sqrt{3}M}{m_p}\right) e^{i\phi_2} .$$

Since the relative phase angles are the important parameters, we can rewrite D^{TR} above for the case of ^{19}Ne as

$$D^{TR} = \alpha_1 \sin\phi_{A,V} + \alpha_2 \sin\phi_{V,W} + \alpha_3 \sin\phi_{A,W} + \alpha_4 \sin\phi_{V,2} + \alpha_5 \sin\phi_{A,2} \quad \text{(II-11)}$$

where

$$\alpha_1 = \frac{1}{\sqrt{3}} \frac{|\rho|}{1+\rho^2} \left(2 - \frac{E_o}{M} + 6\frac{E}{M}\right) \approx 0.518 + \left(0.24 \frac{E}{E_{max}}\right) \times 10^{-3}$$

$$\alpha_2 = -\frac{\mu}{1+\rho^2} \left(\frac{E_o}{m_p} + 2\frac{E}{m_p}\right) \approx \left(0.7 + 7\frac{E}{E_{max}}\right) \times 10^{-3}$$

$$\alpha_3 = \frac{\mu|\rho|}{1+\rho^2} \frac{E}{m_p} \approx -0.2 \frac{E}{E_{max}} \times 10^{-3}$$

$$\alpha_4 = -\frac{\mu_2}{1+\rho^2} \frac{E_o}{m_p} \approx -\mu_2 (0.2 \times 10^{-3})$$

$$\alpha_5 = \frac{1}{3} \frac{\mu_2 |\rho|}{1+\rho^2} \left(\frac{E_o}{m_p} - \frac{2E}{m_p}\right) \approx \mu_2 \left(0.1 - 0.9\frac{E}{E_{max}}\right) \times 10^{-3} .$$

Rewriting Eq. II-11, we have

$$D^{TR} \cong 0.518 \sin\phi_{A,V} + 7\times 10^{-3} \left(\frac{E}{E_{max}}\right) \sin\phi_{V,W} - \mu_2 \times 10^{-3} \left(\frac{E}{E_{max}}\right) \sin\phi_{A,2}$$

$$- 0.2\times 10^{-3} \left(\frac{E}{E_{max}}\right) \sin\phi_{A,W} - \mu_2 \times 10^{4} \sin\phi_{V,2} . \quad \text{(II-12)}$$

The present experiment is predominantly sensitive to a T violation manifesting itself by a phase difference between the vector and axial-vector couplings. This was evident from Eq. II-5 without consideration of momentum transfer-dependent couplings. However, Eq. II-15 demonstrates two important points: (1) there are energy-dependent terms in D^{TR}, and although they are small they are of the same order of magnitude as the final-state corrections D^{EM} (see below); and (2) a complete T violation ($\phi_{ij} = \pi/2$) could occur via vector or axial-vector interferences with either the weak-magnetism or induced-tensor couplings, and go completely undetected at the present uncertainty level.

C. D^{EM} Contributions

It was suggested earlier that final-state electromagnetic interactions can introduce an $\vec{I}\cdot(\vec{p}\times\vec{q})$ correlation into the expression for $d\lambda$. In general, a T-odd observable may arise from (1) a violation of T invariance and/or (2) final-state electromagnetic interactions. Contributions to the coefficient D may arise from both sources.

The Fermi-Watson Theorem[19] states that when final-state interactions accompany a scattering (decay) process, the original scattering (decay) amplitude $\mathcal{M}$ is modified by a multiplicative phase factor $e^{i(\delta-\delta')}$. In the case of ^{19}Ne beta decay, the δ and δ' represent the phases of the original and "Coulomb-scattered" final states.

Applying this theorem to weak decay processes and ^{19}Ne beta decay in particular, it can be shown that the expectation value of a T-odd observable can be factored into two terms,

$$D = \langle \vec{I} \cdot (\vec{p} \times \vec{q}) \rangle = D^{TR} + D^{EM} ,$$

where

$$D^{TR} \propto \cos(\delta - \delta') \, \mathrm{Im}(C_i C_j^*)$$

and

$$D^{EM} \propto \sin(\delta - \delta') \, \mathrm{Re}(C_i C_j^*) \; .^{20}$$

The C_i's and C_j's are the weak-interaction coupling constants.

It is evident that D^{EM} contains no information concerning T invariance. Its magnitude depends upon the phase shift and, in the case of light nuclei ($Z < 50$), $\sin(\delta - \delta') \propto \alpha Z$, where α is the fine-structure constant and Z is that of the daughter nucleus. In the following paragraphs the magnitude of D^{EM} terms (first order in $Z\alpha$) will be given for the zeroth- and first-order terms in the nuclear-recoil parameter $E/2M$. These will be compared to the present experimental uncertainty in D_{exp}.

Jackson, Treiman, and Wyld[16] considered the correction due to simple Coulomb scattering between the daughter nucleus and an electron or a positron in allowed beta decay. Their calculation included momentum-transfer-independent S, V, A, and T weak couplings and neglected nuclear-recoil terms. The result for $I_i = I_f = 1/2$ is

$$\begin{aligned} D_1^{EM} = \frac{2\alpha Z}{\sqrt{3}} \frac{mc}{p} \langle 1 \rangle \langle \sigma \rangle \mathrm{Re} \left| C_S C_A^* - C_V C_T^* + C_S' C_A'^* - C_V' C_T'^* \right| \times \\ \times \Big[\left(|C_S|^2 + |C_S'|^2 + |C_V|^2 + |C_V'|^2 \right) |\langle 1 \rangle|^2 \\ + \left(|C_T|^2 + |C_T'|^2 + |C_A|^2 + |C_A'|^2 \right) |\langle \sigma \rangle|^2 \Big]^{-1} \end{aligned} \qquad \text{(II-13)}$$

which vanishes identically for a pure V-A weak decay. The positron mass and 3-momentum are m and p.

To determine an upper limit for the magnitude of these terms, we may make use of the experimental upper limits of the Fermi and Gamow-Teller Fierz interference terms,[21]

$$b_F = \frac{C_S^* C_V + C_S'^{} C_V' + \text{c.c.}}{\left(|C_V|^2 + |C_V'|^2 + |C_S|^2 + |C_S'|^2\right)}$$

and

$$b_{GT} = \frac{C_T^* C_A + C_T'^{*} C_A' + \text{c.c.}}{\left(|C_A|^2 + |C_A'|^2 + |C_T|^2 + |C_T'|^2\right)} \; .$$

These place the most accurate upper limit upon the S and T couplings in β decay and may be approximated by

$$b_F \cong \text{Re}(s + s') \quad \text{and} \quad b_{GT} \cong \text{Re}(t + t') \; ,$$

where $s = C_S/C_V$, $s' = C_S'/C_V'$. We are justified in this approximation, since measurements of the electron-neutrino angular correlation a in Eq. II-6 established that $|C_S|^2 \ll |C_V|^2$ and $|C_T|^2 \ll |C_A|^2$. Rewriting D_1^{EM} in terms of experimental quantities (assuming ρ is real, i.e., $\cos\phi_{V,A} = 1$), we have

$$D_1^{EM} = \frac{2\alpha Z}{\sqrt{3}} \frac{\rho}{1 + \rho^2} (b_F + b_{GT}) \left(\frac{mc}{p}\right) \; . \tag{II-14}$$

The uniformity of measured ft values in pure Fermi $0^+ \to 0^+$ decays places an upper limit on $b_F < 0.1$.[22] The ratio of K capture to positron emission in the pure Gamow-Teller $3^+ \rightarrow 2^+$ decay of ^{22}Na gives a limit on b_{GT}, $|b_{GT}| < 0.03$.[23] Using $\rho = 1.6$ we obtain

$$D_1^{EM} = D_{Coul.} = 2.2\times10^{-3} \ . \tag{II-15}$$

This represents an upper limit to the correction given in Eq. II-13, and has a characteristic inverse momentum dependence.

In this experiment the positron energy was measured for each event for which the angular correlation $\hat{I}\cdot(\vec{v}\times\hat{q})$ was observed (Sect. III). The energy dependence of D_{exp} was thus experimentally obtained and may be compared to the characteristic energy dependence of each individual final-state correction. Between the threshold and endpoint energies the positron momentum varies between 0.9 and 2.7 MeV/c, giving

$$8\times10^{-4} \leq D_{Coul.} \leq 2.5\times10^{-3} \ .$$

A Coulomb correction, second order in α, has not been calculated but should be of the order of

$$D^{(2)}_{Coul.} \approx \left(\frac{\alpha Z}{p}\right)^2 m_o^2 \approx 5\times10^{-4} \ ,$$

unless there are fortuitous cancellations.

Holstein[24] has calculated, to first order in αZ, the final-state corrections to D which arise from interferences between the momentum-transfer-dependent weak-magnetism and induced-tensor couplings and the Coulomb scattering in the final state. These terms come into play when recoil-dependent terms of the order of $E/2M$ are retained in the expression for the allowed transition amplitude. The result for the

^{19}Ne decay is

$$D_2^{EM} = D_{recoil}(^{19}\mathrm{Ne}) = \pm \frac{\alpha Z}{4pM}\frac{1}{\xi} \times$$

$$\times \left\{ \frac{1}{\sqrt{3}}\,\mathrm{Re}\left[a^*(b\mp c)(p^2+4E_o^2) - a^*dp^2\right] - \frac{1}{3}\,\mathrm{Re}\left[c^*(c\mp b\pm d)(3p^2+4E_o^2)\right]\right\}$$

$$\mp \frac{3\alpha\mu(^{19}\mathrm{F})}{4pM}\frac{1}{\xi}\left\{(a^2-c^2) \pm \frac{2}{\sqrt{3}}\,\mathrm{Re}\; a^*c\right\}p^2 \;, \qquad \text{(II-16)}$$

where the notation is identical to that used above. Only the lower sign refers to the positron decay of ^{19}Ne.

Eq. II-20 includes the final-state correction previously calculated by Callan and Treiman.[25] The weak-magnetism interference terms a^*b and c^*b are the dominant contributions to D_2^{EM}. Evaluating a, b, and d as before, and including only these largest terms, we have

$$D_{\text{weak mag.}} = D_2^{EM}(^{19}\mathrm{Ne}) \approx (2.2\cos\phi_{V,W} + 3.4\cos\phi_{A,W})\left(\frac{p^2+1}{p}\right) \times 10^{-4} \;.$$

Assuming the cosϕ terms are approximately ±1, this becomes

$$D_{\text{weak mag.}} \cong 1.5\times10^{-4}\,\frac{p}{p_{max}} \;, \qquad \text{(II-17)}$$

almost identical in value to the Callan-Treiman result. For experimentally measured events ($0.9\ \frac{\mathrm{MeV}}{c} \le p \le 2.7\ \frac{\mathrm{MeV}}{c}$), D_{wm} varies between 0.4×10^{-4} and 1.4×10^{-4}.

The total final-state correction is then

$$D^{EM} = (2\times10^{-3})\,\frac{1}{p\left(\frac{\mathrm{MeV}}{c}\right)} + (1.5\times10^{-4})\,\frac{p}{p_{max}} \qquad \text{(II-18)}$$

where the first term is an upper limit.

D. Comparison of $|D^{EM}|$ to Experimental Uncertainty

One may conclude that the final-state corrections are small with respect to the present experimental uncertainty in D_{exp} (see Sect. V):

$$\sigma(D_{exp}) = \pm 0.003 \quad \text{(all energies)} ,$$

and can be ignored.

Finally, in the expression for $d\lambda$ (Eq. II-6), we wish to replace the neutrino momenta $\vec{q}$ and solid angle $d\Omega_\nu$ by the recoil-ion momenta $\vec{r}$ and $d\Omega_\nu$. Since the kinetic energy of the neon atoms is less than 0.0025 eV, the laboratory frame and the rest frame of the decaying neon are essentially identical. We have in the lab frame, to good approximation:

$$\vec{p} + \vec{q} + \vec{r} = 0 .$$

Expressing $|\vec{r}|$ as

$$r = |\vec{r}| = -p\hat{p}\cdot\hat{r} \pm \left\{q^2 - p^2[1 - (\hat{p}\cdot\hat{r})^2]\right\}^{1/2} ,$$

one obtains

$$
\begin{aligned}
d\lambda \propto & \left[\frac{pF(Z,E)}{E}\right] E^2 (E_0 - 1)^2 dE\, d\Omega_e\, d\Omega_r\, \frac{r}{q} \\
& \times \left| \frac{-\vec{p}\cdot\hat{r}}{\{q^2 - p^2[1 - (\hat{p}\cdot\hat{r})^2]\}^{1/2}} \pm 1 \right| \\
& \times \left\{ 1 - a\, \frac{p}{qE}(r\hat{p}\cdot\hat{r} + p) + A\, \frac{p}{E}(\hat{I}\cdot\hat{p}) - \frac{B}{q}\, \hat{I}\cdot(\vec{r} + \vec{p}) - D\, \frac{\hat{I}\cdot(\vec{p}\times\vec{r})}{qE} \right\}. \qquad \text{(II-18)}
\end{aligned}
$$

The sign convention refers to the relative sizes of $\underline{p}$ and $\underline{q}$. For $p > q$ and a fixed angle $\hat{p}\cdot\hat{q}$, there are two neutrino momenta $\vec{q}$ for which $\vec{p} + \vec{q} + \vec{r} = 0$. For this reason the total rate is the sum of the rate with the plus sign and the rate with the minus sign.[26] For $p < q$, only the plus sign is applicable. Equation II-18 describes the angular correlations in terms of the particles observed experimentally, and was used to calculate the geometry factors; see Sect. V and Appendix E.

III. EXPERIMENTAL METHOD

This test of time-reversal invariance in beta decay was accomplished by measuring the magnitude of the pseudoscalar triple-angular correlation term $D\{\hat{I}\cdot(\vec{p}\times\vec{r})\}$ in dλ, Eq. II-18. T invariance requires that the coupling constants of the Hamiltonian from which dλ was derived be real, and thus the coefficient D be identically zero.

Experimentally the "D" dependence of dλ is measured by observing those delayed coincidences between e^+ and F^- whose momenta define a plane perpendicular to the spin of the decaying ^{19}Ne. The magnitude of D is measured by taking the difference between the coincidence (decay) rates from states of opposite m_I; i.e., $\hat{I}$ parallel and antiparallel to the normal of the plane defined by the decay products.

Both in the previously reported experimental search for a T violation[1] and in the present experiment, ^{19}Ne is continuously produced in the reaction F(p, n)^{19}Ne. After separation from the carrier gas, a collimated beam of polarized ^{19}Ne is formed with a Stern-Gerlach state-selecting magnet and collimating slits.

In Ref. 1, D was measured by detecting in-flight decays as the neon beam passed two counter arrays. The detection efficiency was low, since neon atoms spent only 10^{-3} sec in the detector region. The coincidence count rate was 1.6 counts/sec. The uncertainty in D was entirely statistical, the result being $D = 0.001 \pm 0.014$.

With the same beam activity in the present experiment, the detection efficiency and thus the coincidence rate was increased several

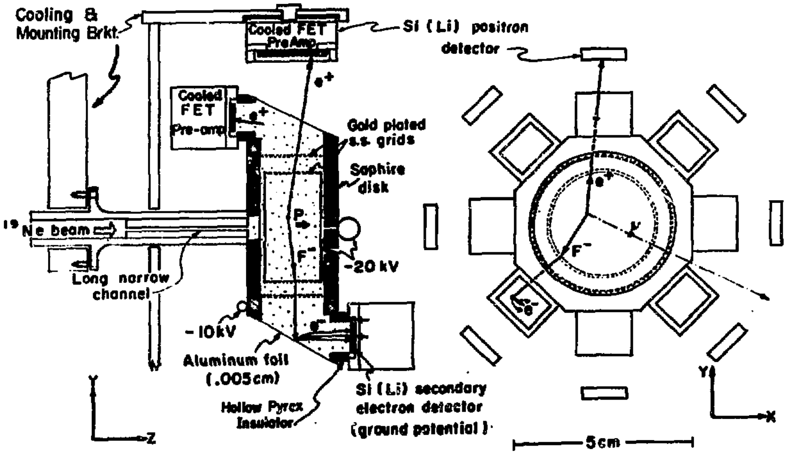

XBL707-3359A

Fig. 1. Side and end view of the octagonal bulb-detector assembly. Converter boxes are shown in the end view as rectangles mounted on the octagon, with openings to the Si detectors alternately facing along the ±z axis. The inner and outer grids are shown as double dashed lines.

After entering the bulb through the long narrow copper channel, the ^{19}Ne atoms (shown as dots) are uniformly distributed throughout the volume of the bulb. The particle trajectories from a typical decay within the inner grid are shown in the both views. The positron passes through the foil, while the ion drifts radially toward the edge of the inner grid. Radial acceleration is followed by secondary electron (e^-) production upon ion impact with foil. The nuclear spin of the ^{19}Ne, denoted as P, is maintained by a magnetic field $\vec{B}_A = \pm\hat{z}|B_A|$. Positrons originating from decays within the converter boxes and passing through the Si (secondary-electron) detectors provide a 500-keV signal. Such a decay is shown at top left. Measuring these 500-keV singles counts provides continuous monitoring of the polarization.

orders of magnitude by trapping, holding, and detecting the activity in a sealed bulb for up to four seconds. The statistical uncertainty was improved by a factor of 5. Paramount in this containment technique is the experimental fact that we are able to maintain the nuclear polarization despite the 10^5 collisions of the ^{19}Ne atoms with the container walls. Counters capable of detecting the recoil F^- ion are an integral part of the sealed bulb, whereas the positrons easily pass through the thin Al foil windows in the bulb to external detectors.

For the "D" experiment, counter geometry design optimizes detection of those delayed coincidence events, between e^+ and F^-, having the T-violating angular correlation described by the D term in Eq. II-18. The spin is maintained parallel to the beam axis (along the z axis in Fig. 1) by a weak axial magnetic field, B_A. Positron and ion detectors are sensitive to events where the positron and ion momenta $\vec{p}$ and $\vec{r}$ are nominally perpendicular to $\hat{I}$, thus providing maximum sensitivity to D. Coincidences are measured for $\vec{p}$ and $\vec{r}$ nominally 90° and 135° apart (Fig. 1).

In the "B" experiment, coincidence counts are observed for those decays having the angular correlation described by the B term in Eq. II-18. The nuclear spin $\hat{I}$ is nominally in the plane formed by $\vec{p}$ and $\vec{r}$. A weak magnetic field perpendicular to the beam axis maintains the transverse orientation of $\hat{I}$.

A. Detailed Description of Apparatus and Operation

The production, separation from the carrier gas, and the polar-

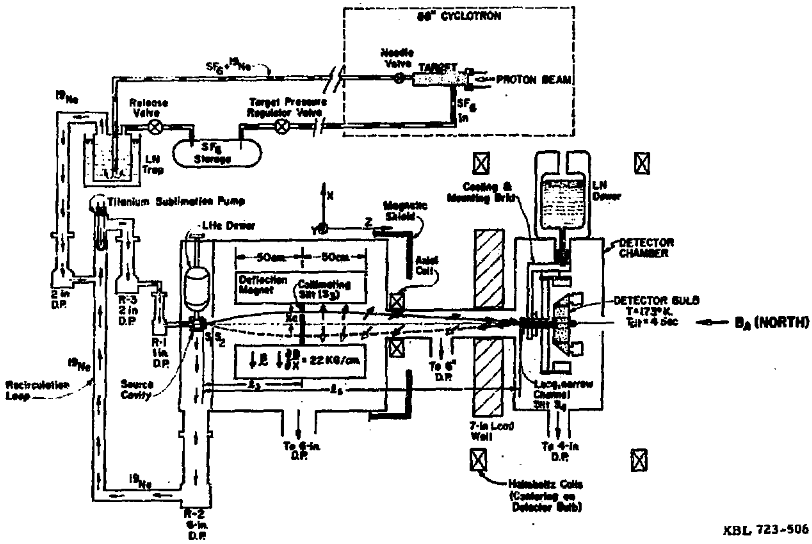

Fig. 2. Schematic diagram of the production, separation from carrier-target gas (SF_6), polarization, and subsequent detection of the ${}^{19}Ne$ activity for the "D" experiment. The target area is separated from the remainder of the apparatus by concrete shielding. A single magnetic substate m_I is selected from the atomic beam of ${}^{19}Ne$ effusing from the source slit S_1 (30°K) in a ${}^1S_0$ state by the collimator slit S_3. The dark (light) arrows represent the orientation of the nuclear magnetic moment of ${}^{19}Ne$ as atoms pass through S_3 for $X_c > 0$ (< 0). The moments adiabatically follow the changing orientation of the magnetic fields. For the orientation of B_A shown and $X_c > 0$, the spins that reach the bulb point along the $-z$ axis. The dark (light) arrows are passed (blocked) for S_3 as shown. The beam is defined by slits S_1, S_3, and S_4. The beam deflections are exaggerated for clarity. The field B_A is produced by the Helmholtz set. (In the "B" experiment, spin alignment in the bulb is maintained by a field B_A along the $\pm x$ axis.) The coils producing this transverse field are not shown. Bulb cooling is provided by contact through the mounting bracket with the LN reservoir. T_{sit} is the sitting time of ${}^{19}Ne$ in the bulb.

ization of ^{19}Ne have been described in detail[1,27] and require only brief mention here. Details not previously described, together with new experimental techniques, will be discussed fully. The entire experimental apparatus is shown in Fig. 2.

1. Production and Separation of ^{19}Ne

A 60-μA beam of 15-MeV protons from the Lawrence Berkeley Laboratory 88-in cyclotron is used to produce radioactive ^{19}Ne. The proton beam enters an SF_6 gas target at 3 atm by passing through a 0.038-cm Ni-plated aluminum foil in the target face. In the reaction[27] $^{19}F(p, n)^{19}Ne$, 10 curies of neon ($\tau_{1/2} = 17.6$ sec) are produced. Rapid delivery of this short-lived activity is essential.

The SF_6 target-carrier gas flows through the target at a rate of 6 (atm-liters)/min, sweeping the neon from the target into one of two LN-cooled traps. Adequate concrete shielding separates the target area from experimental apparatus. Each LN-cooled SF_6 trap consists of a 20-liter copper vessel in which SF_6 is condensed out as a powder onto baffles, leaving only ^{19}Ne to be pumped to the atomic beam source. Total transit time of neon from target to detectors is approximately 5 sec.

Once the SF_6 trap is filled with condensed SF_6, the target gas is diverted into the second SF_6 trap. The experiment may thus continue while the first trap is heated to allow return of its contents to the large SF_6 storage tanks which supply the target. Two traps allow continuous operation.

(following page)

Fig. 3. Details of source, source slits, and source cooling. The source temperature is 30°K. An adjustable bellows mount (not shown) was an integral part of the vacuum flange at the top of the chamber. This bellows mount allowed vertical adjustment of the entire ridged assembly upon which the source cavity was mounted. Horizontal adjustments were made using two externally adjustable S.S. rods which made contact with the foot of the gold-plated copper heat shield. Horizontal and vertical adjustments were critical for precise alignment of the source slits with the deflection magnet center line.

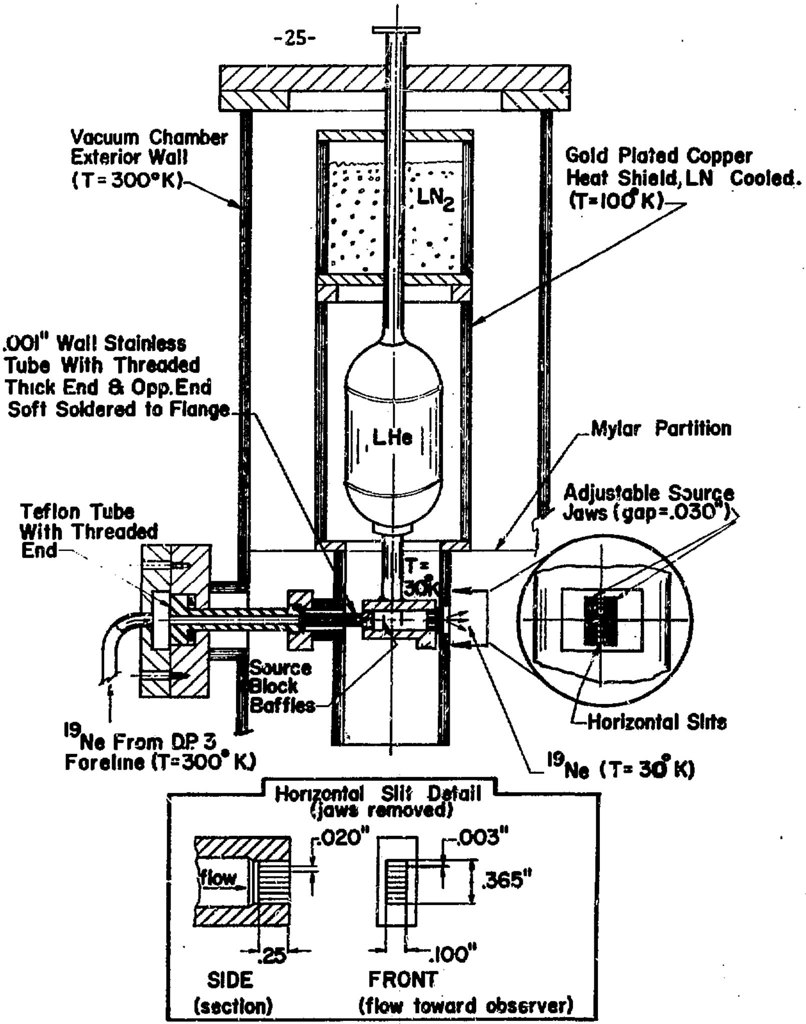

XBL 723-509

Fig. 3. *(see previous page)*

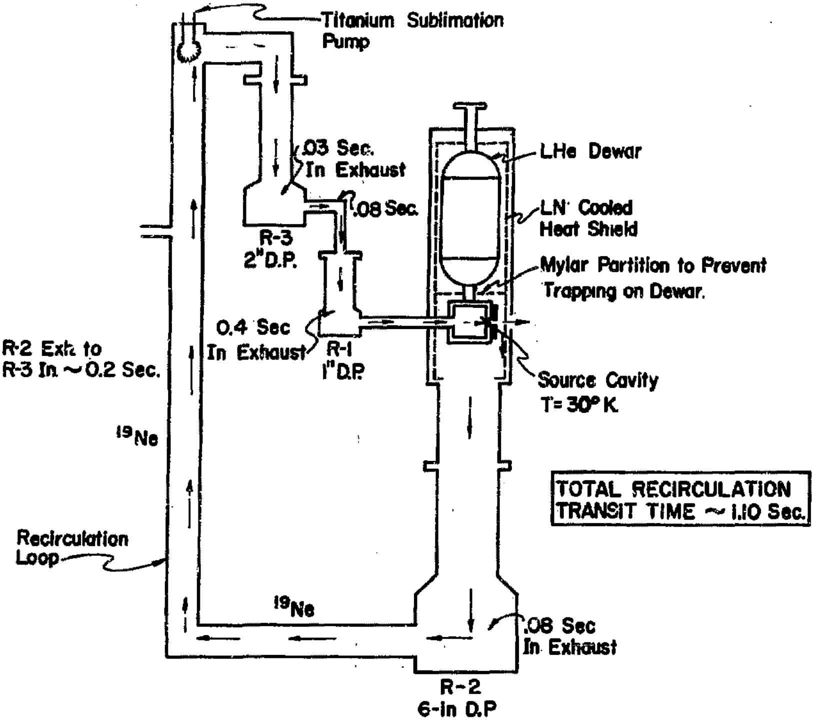

XBL 723-507

Fig. 4. Recirculation loop. The times spent in each segment of the loop are calculated values. With the source at 30°K, S.S. tube at ~60°K, and all other surfaces at 300°K, the times are given in seconds. A factor of between 18 and 20 was gained in beam intensity by reinjecting the gas that did not enter the deflection magnet back into the source.

Injection of the activity into the hollow copper source block occurs after successive compression of the neon by diffusion pumps R-3 and R-1. The source block is cooled to 30°K by the copper mounting rod attached to the base of a LHe reservoir. Source construction and cooling are shown in Fig. 3. To minimize heat conduction between source chamber walls and the LHe reservoir, a Teflon tube plus a stainless steel tube with 0.0025-cm walls connects the exhaust of pump R-1 to the source. A gold-plated copper heat shield, cooled to LN temperatures, surrounds the source and the LHe Dewar. The entire unit is suspended by an adjustable mount in the source vacuum chamber at 10^{-7} Torr.

Neon effuses from the source in the $^1S_0$ ground state through sixteen horizontal slits machined in the source block. These slits are 0.051 cm high, 0.25 cm wide, and 0.64 cm deep (Fig. 3). These horizontal slits and the vertical source jaws labeled S_1 (0.076 cm wide by 0.95 cm deep) channel the beam in the forward direction, increasing the forward beam intensity over that of a cosine distribution by a factor of 15.

Gas not entering the deflection magnet through slit S_2 is pumped from the source chamber and reinjected into the source block via a closed recirculation loop. The activity can thus be circulated up to 20 times before it decays. Using this recirculation scheme, the beam intensity is higher by a factor of 20 than without recirculation.

The time spent in each segment of the recirculation loop is shown in Fig. 4. The factor limiting recirculation enhancement is the low conductivity through the channeling slits. While increasing the

(following page)

Fig. 5. Neon beam profile and polarization at the entrance to the bulb (slit S_4). The solid curves are calculated using $\mu(^{19}\mathrm{Ne}) = -1.88\ \mu_N$, a source temperature of 30°K, and a deflection magnet field gradient of 22 kG/cm, together with the lengths listed in Table I. Experimental points are shown as triangles and squares. X_c is the distance from the magnet center line to the center of S_3. S_3 is 0.076 cm wide. For $X_c \geq 0.076$ cm, the polarization of the beam reaching the bulb is 100%. Arrows indicate locations of the center line of slit S_3 used to select opposite spin states.

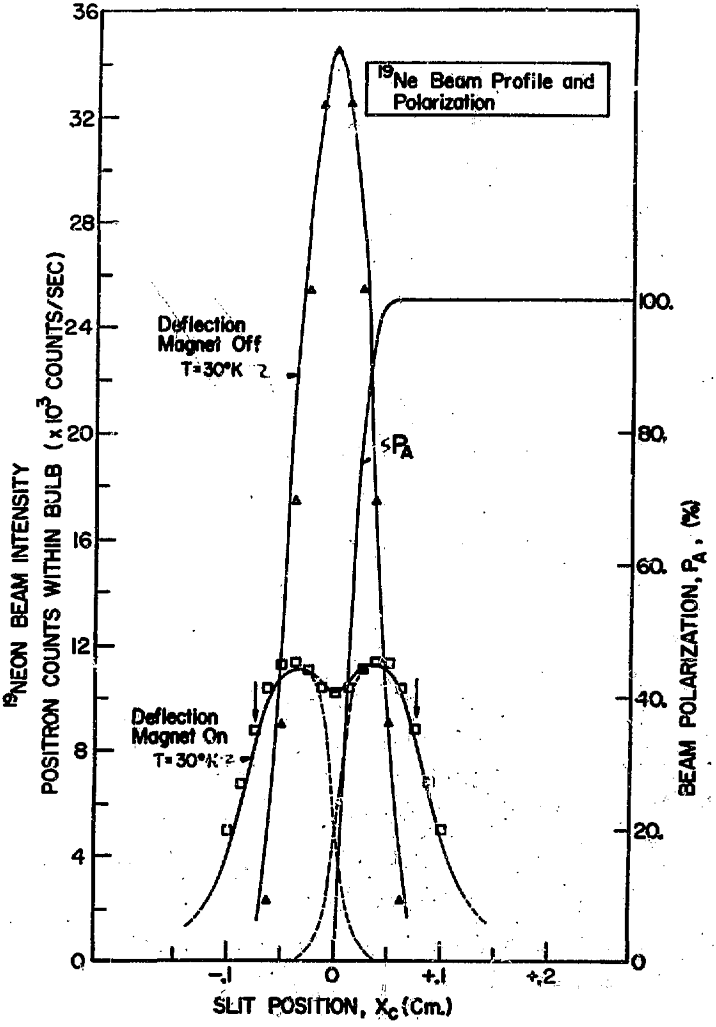

XBL 723-574

Fig. 5. *(see previous page)*

pressure in the source and enhancing the forward distribution of Ne, these slits, at 30°K, limit the rate at which R-1 foreline and the source volumes can be pumped by R-2. Since a large fraction of the recirculation time is spent in R-1 foreline and the source, these volumes must be kept at a minimum to maximize beam intensity.

2. Polarization

Selection of polarization states is shown schematically in Fig. 2. Passing through the 22-kG/cm field gradient of the "Stern-Gerlach" magnet,[28] the two magnetic substates of neon ($m_I = \pm 1/2$) are deflected in opposite directions. With a nuclear magnetic dipole moment $\vec{\mu}(^{19}\text{Ne}) = -1.88\ \mu_N$,[27] the field gradient exerts a force on μ separating the average trajectory of $\mu_I = +1/2$ and $\mu_I = -1/2$ by 0.076 cm at the center of the magnet. Due to the finite width of the slits defining the beam and the distribution of velocities (Maxwell Boltzmann) of the gas emerging from the source, a mixture of spin states exists along the magnet center line (Fig. 5). Selection of a single polarization state is possible by the introduction of a movable 0.076-cm wide collimating slit, S_3. If X_c, the distance from the magnet centerline to the center of S_3, is greater than 0.076 cm, the transmitted beam contains only one substate, i.e., it is 100% polarized. This follows, since $S_1 = S_3 = S_4$ where S_4 is the width of the entrance channel to the bulb.

In the D experiment, spins are rotated adiabatically through an angle of 90° after emerging from the deflection magnet (see Fig. 2). Upon entering the bulb through slit S_4, the spin is parallel to the bulb axis. For $X_c > 0$ ($X_c < 0$) the spin points along the $-Z$ ($+Z$) axes in Fig. 2.

The strong axial coil field (Fig. 2) rotates the spin by ~60° in an average field of 230 gauss during the first 6 inches of flight. The weaker Helmholtz field B_A completes the rotation over a 30-in span in an average field of 22 gauss. The condition ensuring adiabatic passage through a region of changing field is $\Omega \gg \tau$, where Ω is the transit time through the region and τ is the Larmor precession period about the rotating field. For the first abrupt rotation in the strong field, $\Omega \approx 10^{-3}$ sec and $\tau = 10^{-6}$ sec; and for the second slower rotation in the weak field, $\Omega = 5\times10^{-3}$ sec and $\tau = 2\times10^{-5}$ sec. Both satisfy the adiabatic condition; thus a 100% polarized beam enters the bulb. With neon spending up to 4 sec in the bulb, a highly uniform magnetic field was necessary to minimize relaxation of the spin and thus maintain the polarization.

A set of Helmholtz coils, 5 ft in diameter and centered on the bulb, immerse the bulb in a 22-gauss alignment field B_A. The observed variation of this field over the bulb volume was less than 0.2×10^{-3} G. To obtain this level of uniformity all magnetic materials were kept from the detector chamber region. The only exception was the iron magnetic shield between the deflection magnet and the detector chamber. This shield reduced the variation of the deflection magnet's highly nonuniform fringing field to less than 5×10^{-3} G over the bulb region.

Maximum flux of ^{19}Ne into the bulb was achieved by locating the detector chamber directly behind the lead wall which shielded the

Table I. Position, dimension, and flux[a] through slits defining beam.

	Source Slit (S_1)	Collimator Slit (S_3)	Entrance Channel (S_4)
Width (cm)	0.076	0.076	0.076
Height (cm)	1.25	1.00	0.95
Thickness (cm)	0.32	-	7.6
Distance from source slit (cm)	-	67.6	228.
Solid angle (sr)	-	1.6×10^{-5}	1.4×10^{-6}
Estimated flux of ^{19}Ne atoms (atoms/sec)	$\sim10^{11}$	$\sim10^{6}$	$\sim10^{5}$

[a] Fluxes given for collimator slit position at center line of deflection magnet, i.e., at $X_c = 0$.

detectors from the high background radiation in the source block. This proximity of the bulb to the deflection magnet made the iron shield absolutely essential for the reduction of its fringing field to the 5×10^{-3} G level.

With $X_c > 0$ ($X_c < 0$) the spins of the neon gas trapped in the bulb are oriented in the same (opposite) direction as $\vec{B}_A$. To eliminate possible systematic errors, equal amounts of coincidence data were obtained for $\vec{B}_A$ oriented along the +Z axes and -Z axes. This reversal of field was achieved by reversing the current in both the Helmholtz coils and the single axial coil in Fig. 2. A summary of D asymmetries for the two field orientations is given in Table V.

In the "B" experiment the transverse orientation of the emerging spins in the beam is maintained along the $\underline{x}$ axes by a large pair of square coils not shown in Fig. 2. These coils provide (1) an alignment field between the deflection magnet and the bulb, and (2) a highly uniform field throughout the bulb region.

The neon beam fluxes and solid angles are given in Table I. With the bulb properly aligned with respect to the deflection magnet, approximately 28% of the neon beam reaching the detector chamber enters the bulb via the 0.076-cm channel and scatters randomly to produce a uniform distribution of gas throughout the bulb. The neon can make approximately 10^5 wall collisions before it decays or is pumped back out the entrance slit into the vacuum surrounding the bulb. Neon not originally entering the channel is immediately pumped from the detector chamber in a time of the order of 0.1 sec. The sitting time of neon in the bulb is determined by the conductance of the entrance channel and the bulb volume.[35] For large sitting times, $\tau_s \sim 10$ sec, the greater probability of decay [$\tau_{\frac{1}{2}}(^{19}\text{Ne}) = 17.6$ sec] is accompanied by loss of polarization due to wall collisions. A brief discussion of relaxation processes appears in Appendix D. Our choice of a 4-sec sitting time yielded 75% polarization; see Section II-3d.

B. Bulb

1. General Requirements of Bulb

The purpose of the bulb was containment and detection of the neon activity in the beam. The following general considerations were dominant factors in the design of the bulb: (1) A sizable fraction of the polarized ^{19}Ne beam must enter the bulb and remain, without substantial depolarization, for a time long enough for appreciable decay [$\tau_{\frac{1}{2}}(^{19}\text{Ne}) = 17.6$ sec]; (2) To maintain the uniformity of the guide field within the bulb, both the bulb and the detectors must be totally nonmagnetic — nonuniformities induce depolarization of nuclear spin; (3) In order to concentrate the activity and maximize detection efficiency, the size and volume of the bulb must be minimal; (4) The acceleration and detection of the negative recoil ions, without loss of their directional correlation information, requires (a) a field-free region for ion drift and (b) a large high-voltage gradient providing acceleration; and (5) A high degree of rotational symmetry in the geometry of the bulb and detectors is essential to maximize counting of the trapped activity and allow adequate measurement of systematic

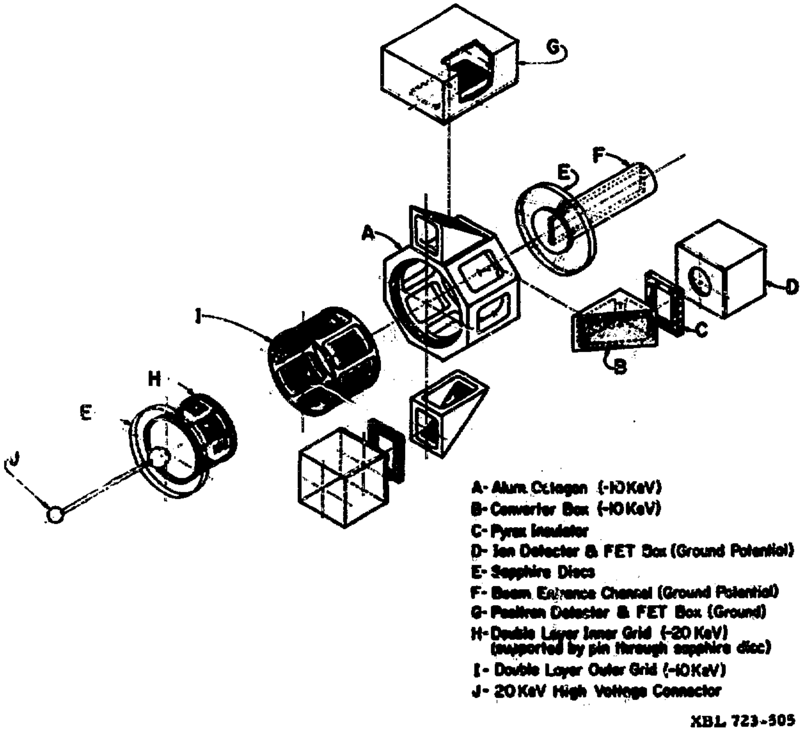

Fig. 6. Exploded view of bulb-detector assembly. The sapphire discs were held onto the octagon by small brass spring clips. The other items were secured with 0-80 screws. All joining surfaces were lapped to flatness. Dow Corning silicon-based vacuum grease was used to ensure a vacuum seal of all joints. A copper lip, threaded into the end of the copper beam entrance channel, secured the sapphire disc. The only opening in the bulb was the 0.076×0.95-cm entrance slit. When all joints were properly sealed the sitting time of the ^{19}Ne in the bulb was 4 sec.

false asymmetries.

2. Bulb Design and Operation

The hollow Al frame (labeled A in Fig. 6) upon which the bulb is constructed forms an octagon 2.54 cm in length, with a centered 4.76-cm I.D. hole along its symmetry axis. (In the following passage, letters labeling bulb components refer to Fig. 6.) Eight equally spaced rectangular parts provide passage to the flat faces of the octagon. Here, facing alternately in opposite directions, Al converter boxes (B) and ion detectors (D) are screwed to the Al frame. Lapping and Si vacuum grease provided vacuum seals between adjoining faces. The top of each converter box, formed from a 0.005-cm Duralumin foil, provides a window through which positrons may leave the bulb. Ions striking the foil stop and eject secondary electrons, which are accelerated, allowing detection of the ion. The foil is glued to the box with Shell epoxy; the curing time and the specific ratio of Shell 828 resin to curing agent D were specific for this low-temperature application.

The ends of the octagon are sealed by sapphire discs (E) 4.76 cm in diameter and 0.22 cm thick, which were grown to order by the Crystal Division of Union Carbide. A vacuum seal between the Al frame is again assured with Dow Corning high-vaccum silicon grease. To prevent prompt loss of the trapped neon into the surrounding vacuum, the entire bulb is vacuum tight except for the narrow copper entrance channel (F), 0.076 cm wide by 0.95 cm high by 7.62 cm long. Positron detectors (G) are mounted externally to the bulb on a carefully machined bracket that ensures the alignment of detectors with the thin windows and the concentricity of the detectors with the bulb.

The inner grid (H) is a hollow metallic cylinder with solid ends. Its sides are constructed from two layers, separated by 0.16 cm of a fine mesh stainless steel screen which is 90% transparent. The gold-plated S.S. screen is composed of sixty fine (0.00025 cm) strands per inch and is manufactured by Buckbee Mears Company. The grid is mounted along the bulb axis by a pin through the center of the sapphire disc; thus it is electrically insulated from the rest of the bulb. Being maintained at -20 keV, the field-free volume within the grid (26% of the bulb volume) defines the region from which delayed coincidence events are accepted. This grid is 1.90 cm long and 3.80 cm in diameter.

Along the inner diameter of the Al octagon the outer grid (I) is formed from a double layer of the same 90% transparent mesh. The radial distance between grids is 1 cm. The outer grid along with the Al octagon and converter boxes is maintained at -10 keV, thus providing a 10-keV/cm potential gradient for the acceleration of F^-. The double-layer construction of the grids reduces undesirable fringing of the field into the interior of the inner grid and converter box. The strong E field at the surface of the inner grid will extract large fluxes of electrons from any microscopic metal whiskers present on the surface of the grid wires. To reduce this field emission, both grids are gold-plated. Examination of the plated surfaces with a microscope showed that all metal whiskers and irregularities on the original grid wire surface had been covered by the gold plate.

The entire bulb-detector unit is held by an Al bracket which is mounted on a brass pedestal inside a 50-liter vacuum chamber (see Fig. 2). The Al bracket is positioned on the pedestal by dowel pins which allow removal and replacement of the bulb-detector unit without loss of the alignment between the entrance channel and the beam axis. The pedestal and Al bracket provide thermal contact between the external LN reservoir and the silicon detectors. Thermal contact to the ion detectors is through the Cu entrance channel and the sapphire end plates. Sapphire is both an electrical insulator and a thermal conductor. Its thermal conductivity and coefficient of expansion are approximately equal to that of copper at LN temperatures.

The pressure in the detector chamber is maintained at 5×10^{-7} Torr by a 500-liters/sec oil diffusion pump. At this pressure, high-voltage breakdown within the bulb was rarely a problem. Careful rounding and polishing of edges and corners of bulb components enabled 20-keV potential differences to be maintained for tolerances of less than 8 mm. To prevent damage to the grids in case of high-voltage breakdown between grids or between grids and ground, 100-MΩ surge-current-limiting resistors were placed in the high-voltage lines. These resistors were 9 mm in diam and 2.5 cm long. Their small size allowed placement within the vacuum chamber between the high-voltage vacuum feedthrough and each grid, thus providing maximum protection.

3. Detection

Both positrons and ions (secondary electrons) are counted with lithium-drifted silicon [Si(Li)] semiconductor detectors made at the Lawrence Berkeley Laboratory. Particles passing through or stopping in the sensitive volume of the detector liberate charge in proportion to energy lost. This charge is swept from the depletion region of the detector by a large bias voltage, producing a charge pulse.

High-energy resolution in the detector systems depends fundamentally upon maximizing the signal-to-noise ratio. To achieve an energy resolution of a few keV, it was essential that (1) the initial stage of preamplification, the field effect transistor (FET), be located close to the silicon detector, and (2) both the detector and the FET be cooled to -100°C. At this temperature the gain of the FET is at a maximum, while the leakage currents in the detector and the FET are reduced by a factor of 200 below room-temperature values. Thermal noise in the feedback resistor is also reduced.

Preamplifier input capacity increases with the distance that separates the detector from the FET. The preamplifier input voltage is maximized by placing the FET and its feedback circuit directly behind the detector in the vacuum chamber. The remainder of the preamplification circuit was mounted outside the vacuum chamber.

Large-amplitude megacycle oscillations, which saturated the scalars, were induced when the feedback response time between the FET and the external preamp circuit was too long. Stable operation of the preamplifier required that cables 33 cm or shorter be used to reduce the transit times of feedback signals.

a. Positron detection. The positron detectors are located outside the sealed bulb. Given the 2.21-MeV positron endpoint energy of ^{19}Ne, the average positron energy is 1 MeV. When escaping from the bulb, a 1-MeV positron loses 11 keV in the converter box foil. Neon gas is uniformly distributed throughout the bulb so decays can occur anywhere inside. Within the inner grid, decays provide possible coincidence events. For decays outside the inner grid, positrons may be counted as singles events in either the positron detectors or the ion detectors (Fig.15). Let these respective singles rates be N_{E_i} and N_{EI_i} in the ith counters. N_{E_i} is the number of positrons passing directly through the thin Si(Li) ion detector for decays within the converter box. Continuous monitoring of the ^{19}Ne polarization is provided by measurement of E_i; this will be discussed in Section III-3d.

Extremely large-volume positron detectors were required to provide both the adequate solid angle and the necessary sensitive range to stop, detect, and measure the energy of positrons with energies up to 2.21 MeV. A triple-angular correlation (TAC) resulting from a final-state interaction has a definite positron-energy (E_e) dependence (see Section II), while a true T-violating TAC is independent of E_e. Measurement of E_e for each coincidence allows us to distinguish these two cases. The dimensions of the sensitive depletion volume are 3.81 cm by 4 mm thick. This thickness provides sufficient range to stop 2-MeV positrons; higher-energy positrons pass through the detector and are recorded as 2-MeV events. The detectors operated with a reversed bias

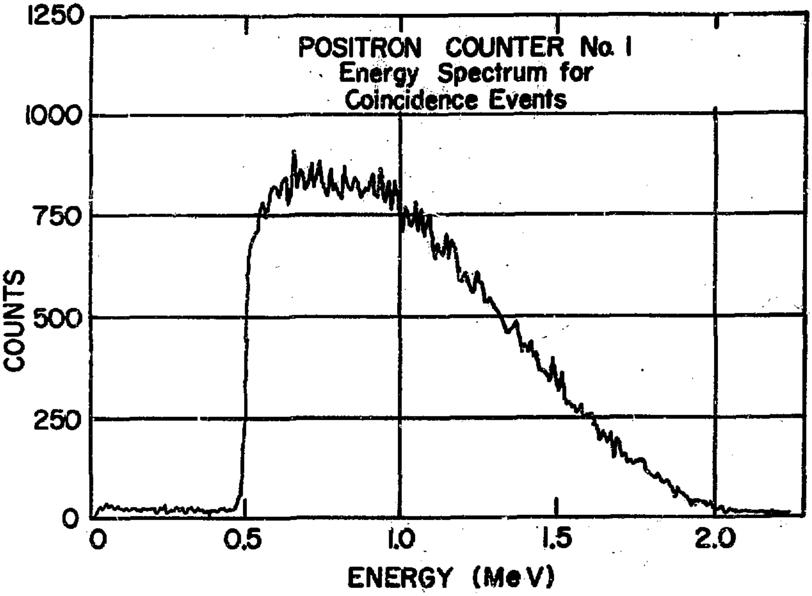

XBL 723-511

Fig. 7a. Measured positron energy spectrum for coincidence events. In both "B" and "D" experiments, the positron energy discriminators were set at 0.5 MeV to eliminate background from the 0.511-MeV positron annihilation gamma rays, γ_{ann}.

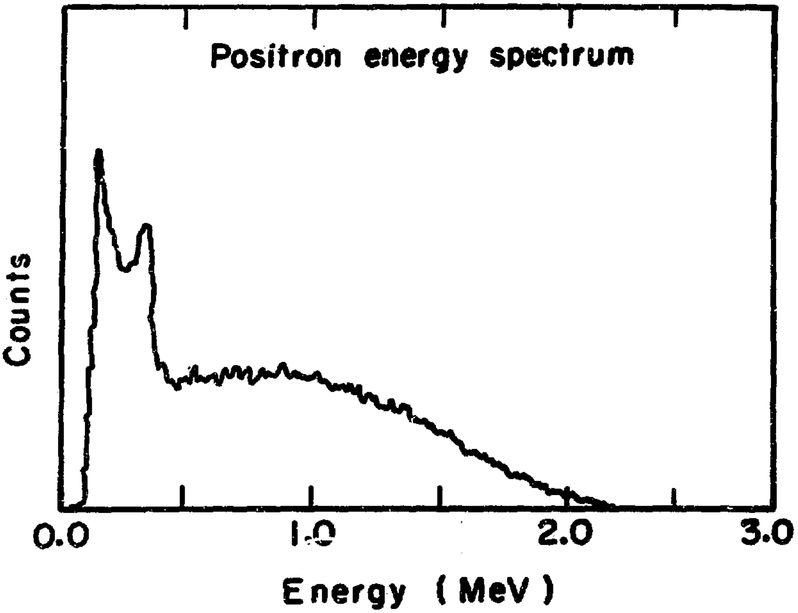

XBL 707-3357A

Fig. 7b. With positron energy discriminators lowered to 0.1 MeV we can observe the energy loss of the γ_{ann} in the Si detector. This appears as a Compton scattering spectrum superimposed on the positron spectra. The sharp peak corresponds to the 340-keV singles Compton-scattering peak produced by γ_{ann}.

voltage of 400 V and had an energy resolution of 9 keV.

A typical coincidence positron energy spectrum is shown in Fig. 7. A ^{137}Cs source providing internal conversion electrons from ^{137}Ba at 625 keV and 655 keV was used for energy calibration. Discriminators were set to accept all positrons above 0.5 MeV. The positron energy is recorded for positrons associated with a coincidence event.

b. Ion detection. Counting the negative recoil ions requires a highly stable, efficient, low-noise detection system which, in contrast to the positron counters, must be an integral part of the sealed bulb. These counters, based on an earlier design,[30] consist of a converter box with a thin secondary-emission Al foil, a Si(Li) detector plus FET, and a hollow glass electrical insulator separating the two (Figs. 1 and 6). The silicon detectors are 1.27 cm in diameter and 1 mm thick, providing sufficient range to stop 600-keV electrons. The sensitive depletion region is 0.96 mm thick. Energy resolution is approximately 4 keV. To maintain the 125-V bias, a 50-Å gold layer was evaporated on the face of the detector through which electrons entered.

A typical coincidence event from a decay within the field-free region of the inner grid is shown in Fig. 1. The positron is detected immediately. The ion, having an average recoil energy of 100 eV, drifts slowly in its original recoil direction toward the transparent surface of the inner grid. Drift times range between 0 and 1.4 μsec. Once the ion has passed through the grid, it is immediately accelerated radially toward the thin window of the converter box, which can collect ions only from this portion of the inner grid surface. Passing through the outer

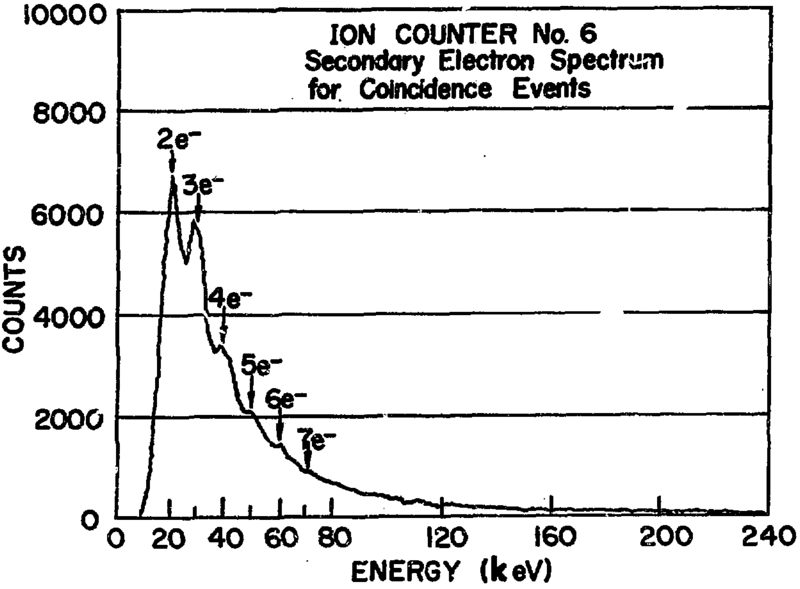

XBL 723-513

Fig. 8. For B and D data the ion energy discriminator was set at 15 keV, to eliminate the large number of single secondary electrons produced by prompt recoil ions (see Sect. V). Prompt coincidence events do not yield valid B or D data. These prompt ions originate from decays between the -10-keV and -20-keV grids and, having less kinetic energy, produce fewer secondary electrons. The presence of the prompts explains the deviations of the spectrum shape from a pure Poisson distribution.

grid, the 10-keV ion collides at a nominal angle of 45° with the Al window and stops. The impact of the ion causes secondary electrons to be ejected from the metal surface.

With the Si detector at ground potential and insulated from the -10-keV converter box, the secondary-emission electrons are to some extent focused and accelerated toward the Si detector. An ion is thus detected as a pulse of one or more 10-keV electrons by the Si ion detector. For decays between the 20- and 10-keV grids, ions are accelerated immediately in the radial direction and detected in the same way. With respect to the positron, these prompt ions are delayed less than ions from the inner grid. Coincidence events originating between grids can be distinguished in this way from those originating from within the inner grid. Let N_{I_j} be the ion singles rate in the j^{th} ion counter.

The frequency distribution of secondary electrons emitted follows Poisson statistics. The average number emitted per stopped ion is equal to the secondary emission coefficient γ: with 10-keV ions on Al at 45°, $\gamma \approx 3$. For one, two, three, etc. electrons ejected, the silicon detector resolves individual lines at 10 keV, 20 keV, 30 keV, etc., as seen in a typical ion coincidence energy spectrum (Fig. 8). The ion discriminator was set at 15 keV, so the two-electron peak is the first one seen in this figure.

It should be noticed in Fig. 8 that the individual peaks broaden as the number of electrons increases. The Si detectors produce this broadening, since statistical fluctuations in charge production for

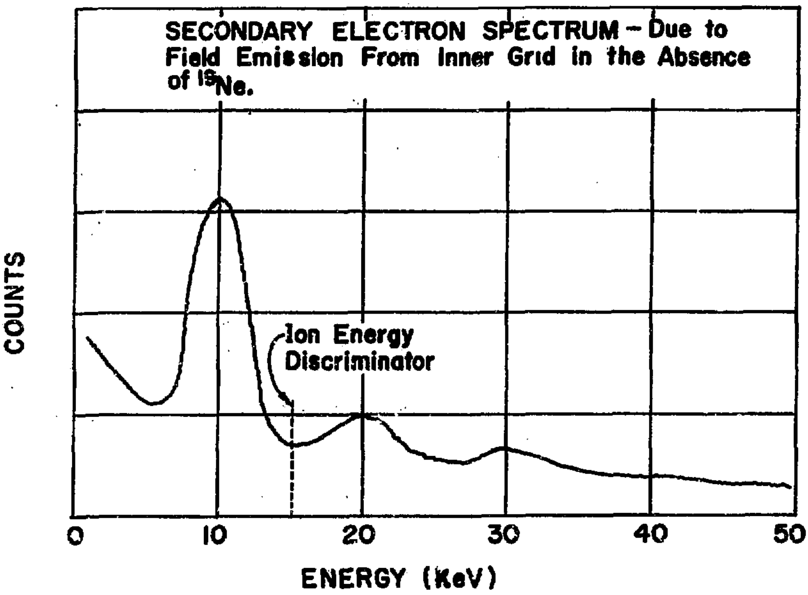

XBL 723-510

Fig. 9. The secondary-electron spectrum due to field emission provided a means of energy calibration of the ion recoil spectra.

individual electrons add in quadrature. Thus the width of the 40-keV peak for four 10-keV electrons is greater by a factor of $\sqrt{4} = 2$ than it would be for a single 40-keV electron.

Noise in the ion counters due to field emission from the inner grid was initially a serious problem. With the large voltage gradient between grids, field emission electrons could be drawn off dust particles and/or metal whiskers on the small-diameter grid wires. These 10-keV field-emission electrons produced an average of one secondary-emission electron upon striking the foil. The secondaries, in the absence of any ^{19}Ne, produce a spectrum in the ion detectors with a large one-electron peak and a smaller two-electron peak (Fig. 9).

The ion counters were totally saturated by these field-emission (and subsequent secondary-emission) electrons. This background was reduced by a factor of 10,000 to an acceptable level, less than 0.1 counts per sec (above 15 keV) per ion counter, by (1) gold-plating the inner and outer grids to provide a microscopically smooth surface free from sharp metal barbs and (2) careful cleaning of the grids in nitric acid, distilled water, and alcohol to eliminate dust and blemishes. This field emission provided an accurate and convenient means of energy calibration for the ion spectra.

4. Polarization Monitoring

During the "D" experiment ($\vec{I}$ along the beam axis), continuous monitoring of the ^{19}Ne polarization is achieved by using the Si ion detectors to measure the angular correlation term $A\hat{I}\cdot\hat{p}\left(\frac{v/c}{I}\right)$ in

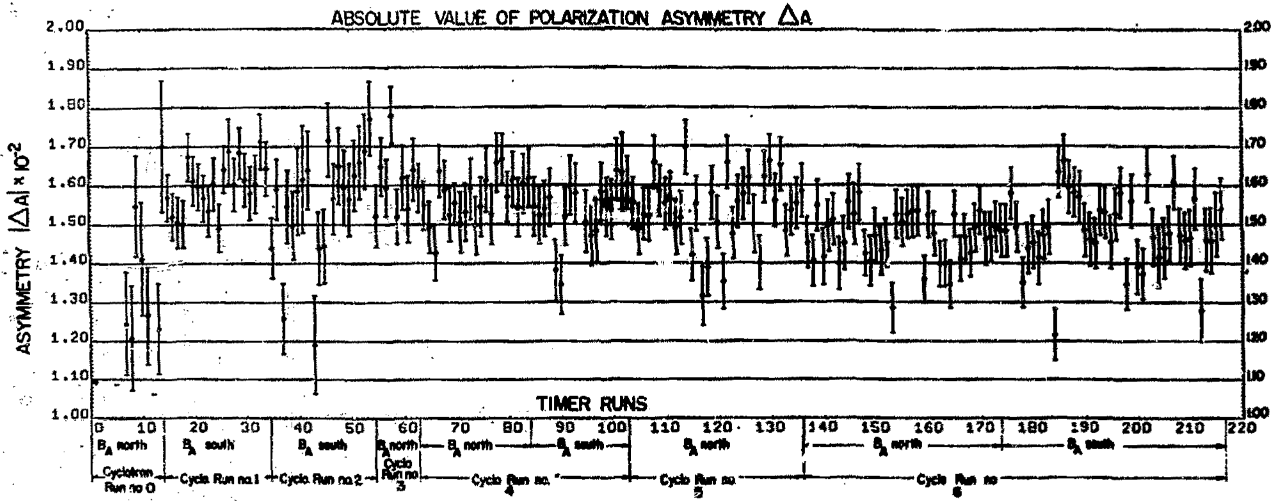

XBL 723-108

Fig. 10. The constancy of $|\Delta_A|$ indicates that the polarization maintained in the bulb did not change significantly either (1) when the alignment field B_A was reversed, or (2) from one cyclotron run to another. $B_A = 22$ gauss in cyclotron runs nos. 1-6. The D data was not used for any timer run whose values of $|\Delta_A|$ deviated by more than $2\sigma_I$ from the experimental average of 1.52 ± 0.01; $\sigma_I \approx 0.15\times10^{-2}$ was the typical error in Δ_A for a single timer run. The Δ_A values for cyclotron run no. 0 were lower than other runs, as the magnitude and uniformity of B_A were less. Run no. 0 data was not used in the B and D experiments.

Eq. II-18. ^{19}Ne decaying inside the converter boxes emits positrons which can pass through the 1-mm silicon ion detectors, producing a high-energy pulse. The energy lost by a 1-MeV to 2-MeV positron is 500 keV, substantially higher than the energy from ion singles. With converter boxes and Si ion detectors alternately facing in upstream-downstream directions along the beam axis, the difference over the sum in the high-energy singles count rates, N_{E_1}, from alternate detectors is proportional to the polarization. Specifically, the polarization is given by

$$P = \frac{1}{A\, S_A\, G_A \left\langle \frac{v}{c} \right\rangle} \Delta_A \qquad \text{(III-1)}$$

where A = 0.039 is the previously measured asymmetry coefficient, $S_A = 0.85$ and $G_A = 0.62$ are the calculated* backscattering correction and geometry factor for this geometry, and $\left\langle \frac{v}{c} \right\rangle = 0.96$ is the average positron velocity between the 0.5-MeV discriminator setting and the 2.21-MeV endpoint energy. Δ_A is defined as

$$\Delta_A = \frac{1}{2}\left\{\left(\frac{N_1 - N_2}{N_1 + N_2}\right)_{X_c>0} - \left(\frac{N_1 - N_2}{N_1 + N_2}\right)_{X_c<0}\right\} \qquad \text{(III-2)}$$

where N_1 (N_2) is the sum of the E_1 singles counts for all the upstream (downstream) Si detectors for a given time in a given polarization state or collimator position X_c. A plot of Δ_A vs timer runs throughout the progress of the experiment indicates the consistence of polarization within the bulb (Fig. 10).

---

* Appendix C.

IV. DATA COLLECTION AND ELECTRONICS

The delayed coincidence rates ${}_{i}n_{j}$ are measured between each positron counter E_i and four ion counters I_j, oriented ±90° and ±135° from E_i. For example, E_1 is in coincidence with I_3, I_7, I_4, and I_6, giving coincidence rates ${}_{1}n_{3}$, ${}_{1}n_{7}$, ${}_{1}n_{4}$, and ${}_{1}n_{6}$ (Table II and Fig. 14). Coincidence rates for a total of thirty-two correlated pairs, four for each positron counter, together with the uncorrelated positron and ion singles rates, are accumulated for 15-min intervals in each of the nuclear polarization states ($X_c > 0$ and $X_c < 0$). A 3-min measurement of the singles background completes each measurement sequence. Singles measurements provide a continuous monitor of counter performance and of the polarization. Typical singles rates are $N_E = 12$ counts per second (cps), $N_I = 200$ cps, and $N_{EI} = 20$ cps.

Recorded for each coincidence event is the detector identification defining the coincidence pair, the time delay Δt between positron and ion, and their respective energies ε_e and ε_I. Thus, coincidence events can be grouped according to their values of Δt, E_e, and ε_I for each individual coincidence pair (Fig. 11).

A schematic outline of the electronics and data transfer system appears in Fig. 12. Its operation is as follows. For each positron above threshold (0.5 MeV) from E_i, a fast logic pulse registers a singles count, sets an identification (ID) register labeling this count as coming from E_i, gates off acceptance of all additional positron coincidence starts, and starts the TAC (time-to-amplitude converter) for the determination of the time delay for a possible coincidence. The

(following page)

Fig. 11. Time-of-flight patterns for 90° and 135° coincidence pairs. For these three figures the positron energies are $0.5 \le E_c \le 2.2$ MeV and the number of secondary electrons accepted ≥ 2. Shaded area shows acceptable coincidence data. The upper and lower delay limits are explicitly given in μsec. Note the difference between those for 90° and 135° pairs. The sharp peaks are due to prompt coincidences. Notice also the improved time separation of the prompt peak from the shaded area for the large 20-kV grid.

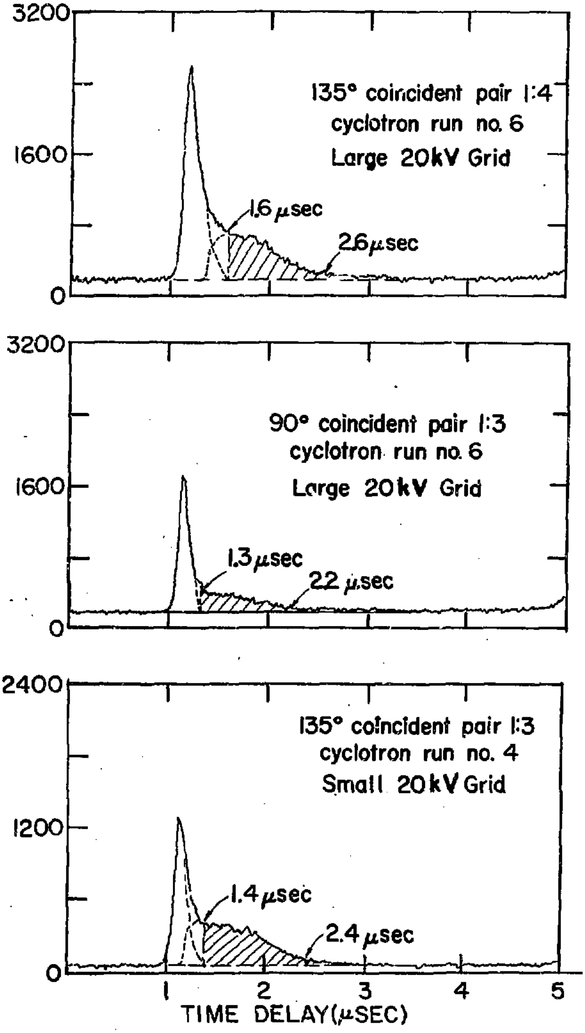

XBL 723-575

Fig. 11. *(see previous page)*

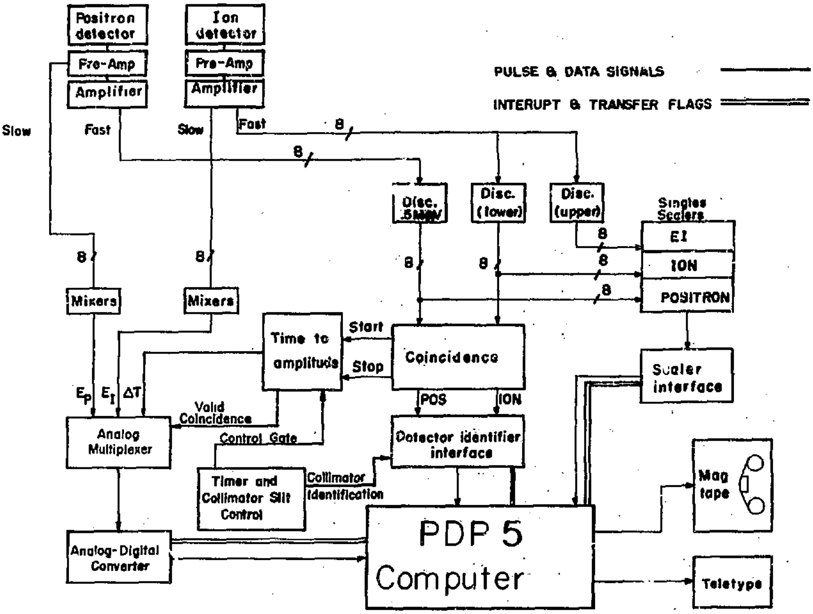

XBL707-3360 A

Fig. 12. Schematic of electronics and data-transfer system. The upper ion discriminator is set at 0.5 MeV; thus the EI singles measures only the passage of positrons through the Si ion detector.

signal level (energy E_e) from the positron preamp is routed to and held in the multiplexer until an ion completes the coincidence. If no coincidence occurs within 5 μsec, the multiplexer and the ID register are each internally cleared and the positron gate is opened.

An ion from I_j provides a fast and a slow linear amplifier output. Above threshold (two secondary electrons = 20 keV), the fast output registers an ion singles count, sets the j^{th}-ion ID register, gates off acceptance of all additional ion coincidence stops, and stops the TAC, thus registering a coincidence. The fast ion pulse also gates the slow ion signal (energy E_I) from the linear amp into the multiplexer.

For a coincidence, the TAC provides the multiplexer with the time delay Δt and a logic pulse labeled 'valid coincidence' in Fig. 12. The multiplexer then interrupts the data analysis of the on-line PDP-5 computer. The PDP-5 initiates serial transfer of the coincidence information — ID registers and multiplexer — into five successive memory buffer locations allotted for each coincidence. When transfer is complete, the computer clears the ID registers and the multiplexer, gates on the positron and ion counters, and returns to a waiting state. After 511 coincidence events the PDP-5 dumps the memory buffer onto magnetic tape.

Simple analysis of the incoming coincidence data is the major source of dead time in the system. The minimum program introduces 23% dead time. A more complete analysis program introduced approximately 50% dead time. For this reason, this longer program was only occa-

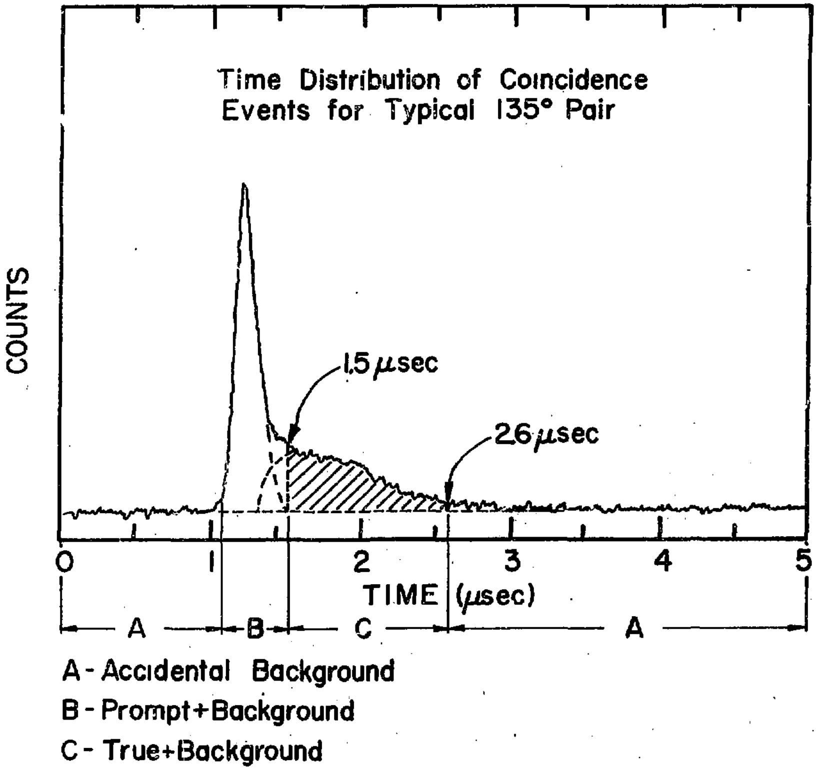

XBL 723-512

Fig. 13. The angular correlation information is lost for prompt coincidence events and cannot be used to measure D. The prompt and true (valid) events overlap in the delay region between 1.2 and 1.5 μsec. Only the events with time delays Δt between 1.5 and 2.6 μsec are true events, i.e., events for which the angular correlation is certain.

sionally used as a check on the performance of all coincidence counter pairs. The long program grouped events which were within preset energy and time-delay limits into an 8×8 coincidence array with indices i and j corresponding to the rates in counter pair ${}_i\eta_j$. This array was printed out on the Teletype after each 15-min run when this longer analysis was used. The singles counts collected during a 15-min run (N_{E_i}, N_{I_i}, N_{EI_i}) were read from the scalers through the computer onto magnetic tape. These singles were always printed out on the Teletype after each 15-min run.

The coincidence gate was held open for 5 μsec accepting ions with delay times between 1 μsec and 6 μsec. Three types of coincidence events occur: prompts, trues, and accidentals. Prompts result from decays occurring between the 10- and 20-keV grids (Fig. 15b). These ions are immediately accelerated in the radial direction regardless of ion recoil direction. Correlation between ion and electron recoil direction is impossible. These events provide no useful D or B information and are sharply peaked between 1.0 μsec and 1.5 μsec (Figs. 11 and 13). True coincidence events result from decays inside the 20-keV grid, where ions drift in their natural recoil direction before acceleration. Correlation information is preserved and delay times range from 1.5 to 2.5 μsec depending on drift path. Prompts and trues can be distinguished since their overlap in time is small (Figs. 11 and 13). Accidental coincidences are uniformly distributed in time. The true events are thus superimposed on a background of accidentals. This background can be measured (and thus eliminated from trues) by holding the coincidence gate open for times before and after which trues are expected

Accidental data was taken for the intervals 0 μsec to 1 μsec and 3 μsec to 5 μsec. Thus, simultaneous measurement of the true and the accidental coincidence rate is achieved.

The true and accidental coincidence rates were 2.5 counts/sec and 0.2 counts/sec, respectively. Considering all coincidence pairs, our true rate was 60 counts/sec. The total time during which good coincidence data was accumulated was approximately 100 hr, although the rate was not always as high as 60 counts/sec.

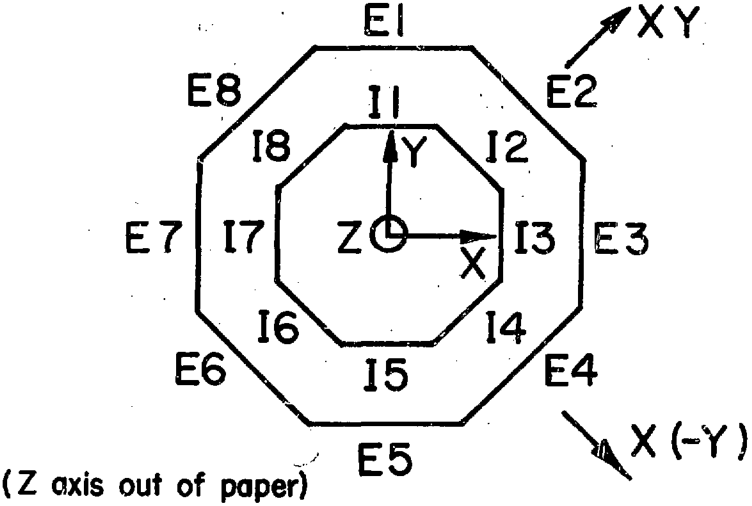

XBL 723-573

Fig. 14. This sketch provides a schematic view of the bulb octagonal counter geometry. Positron and ion counter designations E_i and I_j provide a key to the counter pair numbering in the Table.

Table II. Regular and image coincidence pairs for "D" experiment.[a]

	Pair Index ℓ	Regular	Image	Geometry Factor
135° pairs	1	1:4	1:6	G_D^{135} =
	2	5:8	5:2	0.42 ± 0.03
	3	7:2	7:4	
	4	3:6	3:8	
	5	2:5	8:5	
	6	6:1	4:1	
	7	8:3	6:3	
	8	4:7	2:7	
	9	1:3	1:7	G_D^{90} =
	10	5:7	5:3	0.67 ± 0.03
	11	3:5	3:1	
	12	7:1	7:5	
	13	8:2	2:8	
	14	4:6	6:4	
	15	2:4	4:2	
	16	6:8	8:6	

[a] Coincidence pairs are designated by i:j. i = positron counter; j = ion counter. For each pair i:j the coincidence rate ${}_in_j$ is measured. See Fig. 14 for key to counter pair numbering.

V. DATA ANALYSIS

A. False Asymmetries and Analysis of "D" Data

Misalignment of the field B_A with respect to the bulb axes and differences in coincidence-pair counting efficiencies are two sources of systematic error that can contribute to the magnitude of D. It will be shown that the contribution to D from false asymmetries produced by these two sources of error is less than 1 part in 10^4, i.e., smaller than the statistical error assigned to D by a factor of 10. This follows from the choice of coincidence pairs and the manner in which these pairs are combined to yield D (see Eqs. V-2 and V-3 below). When B_A, and therefore $\vec{I}$, is perfectly aligned along the normal to the detection plane, the "A" and "B" terms in Eq. II-18 average to zero. The "D" term remains, producing an asymmetry in the coincidence rate which depends upon the magnitude of D. Perfect alignment is impossible and, in general, $\vec{I}$ will make an angle α with the normal, thus introducing a component of spin parallel to the detection plane. The B term will not average out as before, and a "false" asymmetry is introduced into the D measurement since B is large ($|B| \approx 1$). The A term will not similarly interfere since $A \approx 0$.

For each coincidence pair an appropriate image pair is chosen. These 16 "regular" and "image" pairs are listed in Table II, where ℓ is the regular-image pair index and i and j designate the positron and ion counters. The measured coincidence decay rate ${}_i n_j$ or n_ℓ for an arbitrary pair is

$$ {}_i\eta_j \approx K\,{}_i\varepsilon_j\left[1 - B\,\frac{\langle I\rangle}{I}\left(\frac{p}{q}\right)(r\hat{I}\cdot\hat{r} + p\hat{I}\cdot\hat{p}) - D\,\frac{\langle I\rangle}{I}\left(\frac{pr}{qE}\right)\hat{I}\cdot(\hat{p}\times\hat{r})\right] \tag{V-1} $$

where ${}_i\varepsilon_j$ is the relative efficiency for the counter pair; p, E, q, and r are the positron momenta and energy and the neutrino and ion momenta; K is a collection of all other factors in the decay rate; and $\frac{\langle I\rangle}{I} = \mathcal{P}$ is the polarization. The sign of the D term is reversed for regular and image pairs.

When the ratios of the difference to the sum of regular (η_ℓ) and image (η'_ℓ) coincidence counts (obtained in one spin state) are summed over ℓ, the false asymmetries due to B and the efficiencies ${}_i\varepsilon_j$ cancel out in first order and enter only as a negligible second-order correction. The resulting number is proportional to the numerical value of D. To minimize spin-independent false asymmetries, the same difference-to-sum ratio ratios for η_ℓ and η'_ℓ are formed for coincidence data taken for equal times in opposite spin states. For each term in the sum over ℓ (i.e., for all appropriate regular and image pairs) these ratios are subtracted. The explicit expressions for the 135° and 90° coincidence pairs are

$$ \begin{aligned} \Delta_D^{135} &= \frac{1}{16}\sum_{\ell=1}^{8}\left\{\left(\frac{\eta_\ell - \eta'_\ell}{\eta_\ell + \eta'_\ell}\right)_{X_c>0} - \left(\frac{\eta_\ell - \eta'_\ell}{\eta_\ell + \eta'_\ell}\right)_{X_c<0}\right\} \\ \Delta_D^{90} &= \frac{1}{16}\sum_{\ell=9}^{16}\left\{\left(\frac{\eta_\ell - \eta'_\ell}{\eta_\ell + \eta'_\ell}\right)_{X_c>0} - \left(\frac{\eta_\ell - \eta'_\ell}{\eta_\ell + \eta'_\ell}\right)_{X_c<0}\right\} \end{aligned} \tag{V-2} $$

where the n_ℓ's are net coincidence counts corrected for accidentals. From Eq. V-1 it is obvious that these Δ's are proportional to the magnitude of D and the nuclear polarization. Explicitly,

$$D = \frac{1}{PS}\left\{\frac{1}{G_D^{90}}\,\Delta_D^{90} + \frac{1}{G_D^{135}}\,\Delta_D^{135}\right\} \tag{V-3}$$

where P is the polarization, S is a backscattering correction (see Section V), and the G's are the geometry factors for the 90° and 135° coincidence pairs (App. E). These geometry factors account for the finite spatial extent of the detectors, the finite decay volume, and the momentum distribution of the decay products.

Calculating D from the coincidence data by this method effectively eliminates counter efficiency differences and interference of the B term only if the misalignment, i.e., $\sin\alpha$, is small (see Appendix A). It is therefore important to determine quantitatively the magnitude of $\sin\alpha$ so an estimate of the completeness of the self-cancellation can be made. The angle α is determined for possible components of B_A along the x, xy, and y axes in the detection plane (see Appendix B). This is achieved by examining those coincidence pairs for which the B term introduces its maximum contribution to the D asymmetry, Δ_D.

The values of α determined in Appendix B for individual cyclotron runs give $\alpha = 2 \pm 1°$, although cumulative results imply that $\alpha \approx 0$.

Using the results of Appendix A, the value $\alpha = 2°$ implies that the second-order contribution to D due to these false asymmetries is indeed $<2\times10^{-4}$, which is a factor of 10 smaller than the statistical uncertainty assigned to D in the present experiment.

B. Analysis of "B" Data

The sets of regular and image pairs defined for the "B" experiment are given in Table III. For the measurement of B the spin lies in the detector plane along the x axis of Figs. 1, 2, and 14. The D term in Eq. II-18 averages to zero, and in general the coincidence rate η depends upon both A and B correlation:

$$\eta \approx K\varepsilon\left[1 + AP\frac{v}{c}(\hat{I}\cdot\hat{p}) - \frac{BP}{q}(r\hat{I}\cdot\hat{r} + p\hat{I}\cdot\hat{p})\right] .$$

With coincidence pairs $\ell = 3, 4$ and 7, 8 we observe both A and B asymmetries. The magnitude of A is known from previous measurements; thus B can be determined from each of the following expressions.

For the 135° pairs:

$$BG_B^1 = \frac{1}{PS}\Delta_B(\ell = 1,\ 2) \tag{V-4}$$

$$\left[BG_B^2 + AG_{B_A}^1\right] = \frac{1}{PS}\Delta_B(\ell = 3,\ 4) \tag{V-5}$$

and the 90° pairs:

$$BG_B^3 = \frac{1}{PS}\Delta_B(\ell = 5,\ 6) \tag{V-6}$$

$$\left[BG_B^4 + AG_{B_A}^2\right] = \frac{1}{PS}\Delta_B(\ell = 7,\ 8)\ , \tag{V-7}$$

Table III. Regular and image coincidence pairs for "B" experiment.[a]

	Pair Index ℓ	Regular	Image	Geometry Factor
135° pairs	1	1:4	1:6	$G_B^1 =$
	2	5:2	5:8	0.48 ± 0.03
	3	4:1	6:1	
	4	2:5	8:5	
90° pairs	5	1:3	1:7	$G_B^3 =$
	6	5:3	5:7	0.77 ± 0.04
	7	3:1	7:1	
	8	3:5	7:5	

[a] Coincidence pairs are designated by i:j. i = positron counter; j = ion counter. For each pair i:j the coincidence rate ${}_i n_j$ is measured. Only pairs ℓ = 1, 2 and ℓ = 5, 6 were used. The geometry factors for the other pairs were not calculated. Pairs ℓ = 1, 2 were used to measure B, while pairs ℓ = 5, 6 were used in the D experiment to measured the misalignment angle α.

where

$$\Delta(\ell) = \sum_{\ell} \left\{ \left(\frac{n_\ell - n_\ell'}{n_\ell + n_\ell'} \right)_{X_c>0} - \left(\frac{n_\ell - n_\ell'}{n_\ell + n_\ell'} \right)_{X_c<0} \right\} .$$

Here n_j and n_j' are the regular and image B coincidence counts obtained in each spin state and corrected for background, while the G's are geometry factors. Since B is known from previous work, the B measurement served only as a check on the design and operation of the bulb. A high degree of accuracy was unnecessary; therefore only the 135° pairs $\ell = 1$ and 2 in Eq. V-4 were used to determine Δ_B.

The 90° coincidence pairs $\ell = 5$ and 6 were used during the D experiment to measure a possible component of B_A along the detector plane $\underline{x}$ axes. Similar 90° pairs were used to detect other components (Appendix B).

C. Results

1. "B" Data

B data were accumulated for a total of ten hours. The value of Δ_B obtained with coincidence pairs $\ell = 1, 2$ (Table III), for all positron energies between 0.5 MeV and 2.21 MeV, and delay times between 1.6 μsec and 2.6 μsec, is

$$\Delta_B^{135} = 0.258 \pm 0.015 .$$

Eq. V-4 with P = 0.75 ± 0.05, S = 0.85 ± 0.1 (Appendix C), and

$G_B^1 = 0.48 \pm 0.03$ (App. E) yields

$$B = -0.85 \pm 0.17 \ .$$

This result is in agreement with the previously measured value $B = -0.90 \pm 0.13$, and indicates proper operation of the bulb-detector system. The uncertainties are attributable to errors in P, G, and particularly S, rather than to statistics.

We have observed that ions can backscatter for grazing angles of incidence. Thus, a combined positron and ion backscattering correction factor $S_e \cdot S_I$ should be used when calculating B and D from the measured Δ_B and Δ_D. Energy and angular distribution data for backscattered positrons is available. An evaluation of S_e for this bulb geometry using this data and Monte Carlo methods is, however, difficult. Only a crude model of positron backscattering was used to estimate the factor S in Appendix C. Little or no experimental data exists for ion scattering; thus, the evaluation of S_I is impossible.

This definitely may be overcome by evaluating the product S_eS_I for the present bulb geometry. Inserting the previously measured value of $|B| = 0.90 \pm 0.13$, and the present value of $(\Delta_B)_{exp}$ into Eq. V-4, we obtain

$$S_eS_I = S = \frac{(\Delta_B)_{exp}}{G_B \ P \ |B|} \ .$$

Inserting the values $P = 0.75$, $G_B = 0.48$, we find

$$S_eS_I = 0.80 \pm 0.04 \ .$$

It is also reasonable to assume that the scattering corrections are the same in the "B" and "D" experiments. We have then

$$(S_eS_I)_D = (S_eS_I)_B = 0.80 \pm 0.14 .$$

Based on experimentally determined quantities, this represents a useful result for the evaluation of the coefficient D below, while S = 0.85 (App. C) used with B data represented little more than an educated guess.

2. "D" Data

We can obtain the value of D for various energy- and delay-intervals by measuring the positron energy and time delay of each coincidence event. The values of Δ_D^{90} and Δ_D^{135} listed in Table IV were obtained by combining the data according to Eq. V-2. The three positron energy intervals into which the coincidence data were grouped are: $\delta E_1 = 0.5$ to 1.0 MeV, $\delta E_2 = 1.0$ to 1.5 MeV, and $\delta E_3 = 1.5$ to 2.21 MeV, where 0.5 MeV is threshold energy and 2.21 MeV the endpoint energy of ^{19}Ne.

For the 90° and 135° coincidence pairs, only those coincidence events with delay times between 1.3 and 2.5 μsec and 1.6 and 2.6 μsec were used to calculated the Δ's. The factors P, S_eS_I, and G_D used to combine the weighted averages of Δ_D^{90} and Δ_D^{135} according to Eq. V-3 are: $P = 0.75 \pm 0.05$, $S_eS_I = 0.80 \pm 0.14$; $G_D^{90} = 0.67 \pm 0.03$ and $G_D^{135} = 0.42 \pm 0.02$ for large inner grid; and $G_D^{90} = 0.77 \pm 0.04$ and $G_D^{135} = 0.56 \pm 0.03$ for small inner grid (Cyc. Run 4). The results are:

Table IV. Computation of Δ_D vs positron energy.[a]

Cyclotron Run #	Orientation of B_A	$2\Delta_D^{135}(\delta E_1)$	$2\Delta_D^{135}(\delta E_2)$	$2\Delta^{135}(\delta E_3)$	$2\Delta^{90}(\delta E_1)$	$2\Delta^{90}(\delta E_2)$	$2\Delta^{90}(\delta E_3)$
1	+Z (South)	+.0030±.0110	-.0046±.0117	+.0142±.0213	-.0135±.0168	-.0109±.0242	+.0728±.0627
2	+Z	-.0133±.0104	+.0148±.0105	-.0040±.0221	-.0157±.0160	+.0055±.0228	+.0552±.0695
3	-Z (North)	+.0083±.0144	+.0196±.0147	-.0101±.0313	-.0378±.0233	+.0123±.0338	-.1021±.1087
4	-Z	-.0014±.0081	+.0080±.0083	+.0188±.0175	-.0063±.0133	-.0139±.0194	-.1518±.0635
	+Z	+.0019±.0093	+.0092±.0095	+.0212±.0202	+.0059±.0149	+.0078±.0217	+.0838±.0648
5	-Z	+.0013±.0073	+.006772±.0081	+.0049±.0257	-.0123±.0110	+.0129±.0184	+.0605±.0808
6	-Z	+.0091±.0105	-.0065±.0097	-.0291±.0183	-.0082±.0172	-.0183±.0228	-.0040±.0628
	+Z	-.0040±.0097	-.0006±.0092	+.0115±.0171	-.0050±.0160	+.0364±.0214	+.0539±.0596
Weighted Ave. for Cyc. Run #4 only[b]		+.0013±.0073	+.0068±.0081	+.0049±.0257	-.0123±.0110	+.0129±.0184	+.0605±.0808
Wtd. Ave. for Cyc. Runs 1-4 and 5-6[b]		-.0002±.0038	+.0048±.0038	+.0045±.0076	-.0088±.0061	+.0020±.0086	+.0113±.0253

[a] δE_1 = 0.5 MeV to 1.0 MeV
δE_2 = 1.0 MeV to 1.5 MeV
δE_3 = 1.5 MeV to 2.21 MeV

[b] Cyclotron Run #4 used small inner grid, while in other Runs large grid was used. The geometry factors for the two cases are different; therefore the Δ's must not be combined.

$$D(SE_1) = -0.009 \pm 0.006$$

$$D(SE_2) = +0.008 \pm 0.005$$

$$D(SE_3) = +0.010 \pm 0.011 .$$

No energy-dependent trend or significant (2σ) difference exists between these D's, implying the absence of any contribution of a final-state interaction to the D data at the present level of sensitivity.

Either by combining the D's above or by taking the weighted averages of Δ_D^{90} and Δ_D^{135} for all energies between threshold and endpoint (listed in Table V), the final result is

$$D = 0.001 \pm 0.003 . \qquad \text{(V-8)}$$

This result is consistent with D = 0. The error in D is purely statistical. The result (Eq. V-8) is based on 100 hours of actual coincidence data accumulation.

3. Polarization Data

Using the EI singles data, obtained continuously during the course of the D experiment, and Eq. III-2, the polarization asymmetry Δ_A was calculated for each 35-min data-taking cycle. The absolute values of these Δ_A's for all cyclotron runs are shown in Fig. 10. The weighted averages for each orientation of B_A are listed in Table VI. Inserting the overall weighted average from Table VI, the previously measured value of $|A| = 0.039 \pm 0.002$, and the values

Table V. Computation of Δ_D for all positron energies.

Cyclotron Run #	Deflection Field	Bulb Alignment Field B_A	Direction of Spin in Bulb $X_c > 0$	$2\Delta_D^{135}$	$2\Delta_D^{90}$
1	-X	+Z (South)	+Z	-.0013±.0075	-.0055±.0136
2	-X	+Z	+Z	-.0000(4)±.0070	-.0059±.0129
3	-X	-Z (North)	-Z	+.0111±.0098	-.0340±.0189
4	-X	-Z	-Z	+.0053±.0055	-.0085±.0108
	-X	+Z	+Z	+.0051±.0063	+.0117±.0121
5	-X	-Z	-Z	+.0029±.0053	-.0041±.0094
6	-X	-Z	-Z	-.0024±.0067	-.0123±.0135
	-X	+Z	+Z	-.0020±.0063	+.0121±.0126
		Weighted Average for Cyclotron Run 4 only		+.0029±.0053	-.0041±.0094
		Weighted Average for all other Cyclotron runs		+.0019±.0025	-.0034±.0049

Table VI. Weighted averages for each orientation of B_A.

Cyclotron Run #	Alignment Field	$\|\Delta_A\|\times10^{-3}$	Polarization
1	+Z (South)	1.59±.014	78.4%
2	+Z	1.57±.023	77.5
3	-Z (North)	1.61±.027	79.2
4	-Z	1.56±.015	77.0
	+Z	1.53±.018	75.4
5	-Z	1.54±.012	75.8
6	-Z	1.47±.010	72.1
	+Z	1.50±.012	74.0
Overall Weighted Average:		1.52±.005	74.8%

$$G_A = 0.64$$

$$S_A = 0.85$$

$$v/c = 0.95$$

into Eq. III-1 , we obtain the average polarization

$$P = 75 \pm 5\%$$

where the major uncertainty is S_A.

VI. CONCLUSION

From the final value of D,

$$D(^{19}\text{Ne}) = 0.001 \pm 0.003 ,$$

one obtains from Eq. II-9 the value of the vector-axial vector phase angle,

$$\phi_{A,V} = 180.1 \pm 0.3^\circ .$$

This represents a factor of 5 improvement over the previous result. The quoted error is purely statistical.

Although $\phi_{V,A}$ is consistent with π, implying the relative reality of C_V and C_A, the implication for time-reversal invariance is ambiguous, since both T invariance and the charge-asymmetry condition (Eq. II-4) impose the same relative phase condition on C_V and C_A. T could be violated and $\phi_{V,A}$ exactly equal to π, provided charge symmetry holds. There exists, however, little evidence for the validity of the charge symmetry condition. The observation of second-class weak couplings would directly exclude it from consideration and the ambiguity would vanish. We will assume that charge symmetry is not strictly valid, and thus the measurement of $\phi_{A,V}$ bears directly on time-reversal invariance. The conclusion then, for ^{19}Ne, is that T is conserved in the V, A coupling to within 3 parts in 10^3.

A. Discussion

Until independent experimental evidence of the existence of second-class couplings exists, a totally unambiguous test of T invariance can only be made by the observation of a D-like angular correlation arising from an interference between a first- and a second-class coupling.* Observation of such an interference would immediately invalidate the charge symmetry condition and allow unambiguous interpretation of phase measurements in terms of T invariance alone. Such an interference term could be observed in a pure Gamow-Teller transition, where the expression for D^{TR} given in Eq. II-10 reduces to

$$D^{TR} = \mp \frac{1}{\xi} \frac{2}{3} \operatorname{Im} c^{*} \left[(d + b) \frac{E_o}{2M} - d \frac{E}{M} \right] \quad .$$

Measurement of the energy dependence of D^{TR} for such a transition is dependent only upon first-second class interference. The size of such a term could be of the order of 10^{-3}. Measurement of a term of this size could be impossible, however, due to final-state E-M correction terms of comparable size.

---

[*] It should be noted that, for analogue decays, the induced-tensor coupling is second class. On the other hand, the presence of the induced-tensor term for non-analogue beta transitions does not automatically imply the presence of a second-class coupling since, according to the impulse approximation, first-class terms contribute to d.[31]

APPENDIX A

ELIMINATION OF SYSTEMATIC "FALSE" ASYMMETRIES IN "D" MEASUREMENT

With the high degree of rotational symmetry present in the D experiment, systematic false asymmetries due to detector efficiency differences and spin misalignment cancel out to second order in the expansion of Δ_D. It will be shown here that this cancellation obtains when Δ_D is defined as in Section V. Let α be the angle between the magnetic field or spin and the normal to the detection plane. The detector plane is the x-y plane in Fig. 1. Further, let the component of spin in the detector plane lie along the $\underline{x}$ axis of Fig. 1, i.e., $\vec{I} = I \sin\alpha\, \hat{i} + I \cos\alpha\, \hat{k}$. The coincidence decay rate is

$$ {}_i\eta_j \approx K\, {}_i\varepsilon_j \left\{ 1 + A \frac{v}{c} \frac{\langle I \rangle}{I} \sin\alpha\, \hat{i}\cdot\hat{p} - \frac{B}{q} \frac{\langle I \rangle}{I} \sin\alpha\, (r\hat{i}\cdot\hat{r} + p\hat{i}\cdot\hat{p}) \right. $$
$$ \left. - D \frac{r}{q} \frac{v}{c} \frac{\langle I \rangle}{I} \cos\alpha\, \hat{k}\cdot(\hat{p}\times\hat{r}) \right\} $$

where $\frac{\langle I \rangle}{I} = P$ is the polarization, p and v are the positron momentum and velocity, r and q are the ion and neutrino momentum, i and j refer to the positron and ion detector and ${}_i\varepsilon_j$ the relative coincidence-pair efficiency for i and j. Since $B \approx 1$ and $A \approx 0$, the A term can be neglected.

The coincidence rates for the regular and image pairs in Table II will be divided into four groups and designated by the pair index ℓ. The 135° pairs comprise group I, $\ell = 1, 4$ and II with $\ell = 5, 8$; while the 90° pairs are III, $\ell = 9, 12$, and IV, $\ell = 13, 16$. Only group I will be considered here since cancellations of false asymmetries from Δ_D occur in identical fashion in each group. For individual pairs in I, we can simplify ${}_i\eta_j$ above by averaging over angles and decay volume. For the spin state $X_c > 0$, and the alignment field B_A pointing North, we have:

$$
\begin{aligned}
{}_i\eta_j &= \eta_\ell \\
{}_1\eta_4 &= \eta_1 = {}_1\varepsilon_4\,(1 - b - d) \\
{}_1\eta_6 &= \eta_1' = {}_1\varepsilon_6\,(1 + b + d) \\
{}_5\eta_8 &= \eta_2 = {}_5\varepsilon_8\,(1 + b - d) \\
{}_5\eta_2 &= \eta_2' = {}_5\varepsilon_2\,(1 - b + d) \\
{}_7\eta_2 &= \eta_3 = {}_7\varepsilon_2\,(1 - b' - d) \\
{}_7\eta_4 &= \eta_3' = {}_7\varepsilon_4\,(1 - b' + d) \\
{}_3\eta_6 &= \eta_4 = {}_3\varepsilon_6\,(1 + b' - d) \\
{}_3\eta_8 &= \eta_4' = {}_3\varepsilon_8\,(1 + b' + d)
\end{aligned}
$$

where

$$
\begin{aligned}
b &= B\,\sin\alpha\,\frac{\langle I\rangle}{I}\,\frac{r}{q}\cdot g_1 \\
b' &= B\,\sin\alpha\,\frac{\langle I\rangle}{I}\,\frac{rg_1 - pg_2}{q} \\
d &= D\,\frac{vr}{cq}\,\cos\alpha\,\frac{\langle I\rangle}{I}\,g_3\ .
\end{aligned}
$$

The g's are geometry factors resulting from the averages taken above.

With the z component of spin reversed, $X_c < 0$, the orientation of the component of spin lying in the detection plane is also reversed. The expressions for η_ℓ are identical except the signs of the b, b', and d terms are all reversed. The group I portion of Δ_D^{195} is

$$I_{\Delta_D^{135}} = \frac{1}{8} \sum_{\ell=1}^{4} \left\{ \left(\frac{n_\ell - n'_\ell}{n_\ell + n'_\ell} \right)_{X_c>0} - \left(\frac{n_\ell - n'_\ell}{n_\ell + n'_\ell} \right)_{X_c<0} \right\}$$

or, substituting the above expressions for n_ℓ,

$$8\left(I_{\Delta_D^{135}}\right) = \frac{x_1 - (b + d)}{1 - x_1(b + d)} - \frac{x_1 + (b + d)}{1 + x_1(b + d)}$$

$$+ \frac{x_2 + (b - d)}{1 + x_2(b - d)} - \frac{x_2 - (b - d)}{1 - x_2(b - d)}$$

$$+ \frac{x_3(1 - b') - d}{(1 - b') - x_3 d} - \frac{x_3(1 + b') + d}{(1 + b') + x_3 d}$$

$$+ \frac{x_4(1 + b') - d}{(1 + b') - x_4 d} - \frac{x_4(1 - b') + d}{(1 - b') + x_4 d}$$

where

$$x_1 = \frac{{}_1\varepsilon_4 - {}_1\varepsilon_6}{{}_1\varepsilon_4 + {}_1\varepsilon_6}, \quad x_2 = \frac{{}_5\varepsilon_8 - {}_5\varepsilon_2}{{}_5\varepsilon_8 + {}_5\varepsilon_2}, \quad x_3 = \frac{{}_7\varepsilon_2 - {}_7\varepsilon_4}{{}_7\varepsilon_2 + {}_7\varepsilon_4}$$

and

$$x_4 = \frac{{}_3\varepsilon_6 - {}_3\varepsilon_8}{{}_3\varepsilon_6 + {}_3\varepsilon_8}.$$

Observing the values of ${}_i\varepsilon_j$ given in Table VIIa, it is seen in Table VIIb that the x_k's << 1. The values of b, b' (for small angles α), and d are also << 1. We can expand and simplify the expression for Δ_D^{135} by disregarding terms of fourth order and higher in these small quantities. The result is

Table VIIa. Measured relative coincidence-pair efficiencies for "D" experiment.

Group I	$1^{\varepsilon}4$	$1^{\varepsilon}6$	$5^{\varepsilon}8$	$5^{\varepsilon}2$	$7^{\varepsilon}2$	$7^{\varepsilon}4$	$3^{\varepsilon}6$	$3^{\varepsilon}8$
	.99	.98	.97	1.00	.99	.99	.98	.90

Group II	$2^{\varepsilon}5$	$8^{\varepsilon}5$	$6^{\varepsilon}1$	$4^{\varepsilon}1$	$6^{\varepsilon}3$	$8^{\varepsilon}3$	$4^{\varepsilon}7$	$2^{\varepsilon}7$
	1.00	.81	.97	.88	.92	.71	.89	.94

Group III	$1^{\varepsilon}3$	$1^{\varepsilon}7$	$5^{\varepsilon}7$	$5^{\varepsilon}3$	$3^{\varepsilon}5$	$3^{\varepsilon}1$	$7^{\varepsilon}1$	$7^{\varepsilon}5$
	.86	.92	.95	.89	.96	.89	.92	1.00

Group IV	$8^{\varepsilon}2$	$2^{\varepsilon}8$	$4^{\varepsilon}6$	$6^{\varepsilon}4$	$2^{\varepsilon}4$	$4^{\varepsilon}2$	$6^{\varepsilon}8$	$8^{\varepsilon}6$
	.79	.79	.96	.96	.99	.99	1.00	1.00

Table VIIb. Calculated ratios of measured relative coincidence-pair efficiencies for "D" experiment.

	group I	group II	group III	group IV
x_1	+0.0056	+0.102	-0.0302	0.
x_2	-0.0138	+0.0446	+0.0302	0.
x_3	-0.00477	+0.1293	+0.0391	0.
x_4	+0.00506	-0.0225	-0.0390	0.

$$8\left({}^{I}\Delta_D^{135}\right) = -2\left\{d(1 - x_1^2) + b(1 - x_1^2) + d(1 - x_2^2) - b(1 - x_2^2) + d\,(1 - x_3^2) + (1 - x_4^2)\;\frac{1}{1 - b'^2}\right\}$$

or

$$\Delta_D^{135} = -d\left\{1 - \frac{(x_1^2 + x_2^2 + x_3^2 + x_4^2)}{4} + \left[2 - (x_3^2 + x_4^2)\right]\frac{b'^2}{4} + \cdots\right\} - \frac{b}{4}\,(x_2^2 - x_1^2) + \cdots \, . \qquad \text{(A-1)}$$

The superscript I is dropped from Δ, since this expression holds for each group, only the values of b and b′ changing slightly. The value of d depends slightly on the group, but we are not concerned with this here.

If there exists no difference in detector efficiencies, which is indeed the case in group IV, $x_1 = x_2 = x_3 = x_4 = 0$, and

$$\Delta_D^{135} = -d\left[1 + \frac{b'^2}{2} + \cdots\right] .$$

To determine the magnitude of this second-order correction to d, let $B = 0.88$, $\alpha = 4°$, and $P = 0.75$. Estimating the value of $\dfrac{\langle r\rangle g_1 \mp \langle p\rangle g_2}{\langle q\rangle}$ (i.e., the factors in b′ for I and IV) to be 0.05 and 0.5 respectively, we obtain

$$3\times10^{-6} < \frac{1}{2}\,b'^2 < 3\times10^{-4} .$$

Thus the largest correction to D is a factor of 10 smaller than the statistical uncertainty in our present measurement of D and can be ignored.

Inserting the values of x_i from Table VIIb in the expression for Δ_D above, the b and b' corrections to D are of the order of 2×10^{-4} or smaller. Thus, false asymmetries due to misalignment angles ≤ 4° and the present detector efficiency differences are insignificant in the present experiment.

APPENDIX B

MAGNITUDE OF SPIN MISALIGNMENT DURING "D" EXPERIMENT

A misalignment of the field $\vec{B}_A$ with respect to the $\underline{z}$ axes introduces a component of nuclear spin, I sinα, into the detector plane — the x-y plane of Figs. 1 and 14. In this case the B term in dλ no longer averages to zero and a B-like asymmetry is introduced into the D data. The magnitude of this false asymmetry δ_M, defined as

$$\delta_M = G_B\, B\, \frac{\langle I \rangle}{I} \sin\alpha \;, \qquad \text{(B-1)}$$

is determined by taking the difference over the sum of coincidence rates for appropriate coincidence pairs. Since we are looking for a B asymmetry in D data, the pairs offering maximum sensitivity to a projection of $\hat{I}$ along the $\underline{x}$ axes or $\underline{y}$ axes are simply those that would be used to measure B when $\vec{I} = |I|\hat{i}$ or $|I|\hat{j}$.

The magnitude of δ_M is determined from the expression

$$\delta_M = \frac{Z - Y}{Z + Y} \;,$$

where Y and Z are defined as follows for detection of a component of $\vec{I}$ along the $\underline{y}$ axes:

$$Y = {}_3n_1 + {}_7n_1$$
$$Z = {}_3n_5 + {}_7n_5 \;;$$

the x-y axes:

$$Y = {}_4n_2 + {}_8n_2$$
$$Z = {}_4n_6 + {}_8n_6 \;;$$

the $\underline{x}$ axes:

$$Y = {}_1n_3 + {}_5n_3$$
$$Z = {}_5n_7 + {}_1n_7 \;;$$

or the x (-y) axes:

$$Y = {}_2n_4 + {}_6n_4$$
$$Z = {}_2n_8 + {}_6n_8 \;.$$

The ${}_in_j$ are coincidence counts for the i, j positron and ion counters. The pairs used for the $\underline{x}$ axes are just those listed as $\ell = 5$ and 6 in Table III for the B experiment. These four axes were used to check the self-consistency of the results. All of the rates listed above are for 90° coincidence pairs. When using Eq. B-1 to obtain $\sin\alpha$ from δ_M, the same geometry factor G_B ($= G_B^3$ of Table III) applies for all axes.

The results are summarized in Table VIII in terms of the angle between the $\underline{z}$ axes and $\vec{I}$ when $\vec{I}$ lies in a plane defined by $\hat{z}$ and one of the four detector plane axes listed above. The uncertainty in the angle thus determined is seen to be approximately 2° for individual cyclotron runs and 1° for the combined "North" or "South" runs. The error is purely statistical.

The magnitudes of these measured angles justify the applicability of the results of Appendix A to the present experiment.

Table VIII. Summary of misalignment angles.

Cyclotron Run No.	Alignment Field B_A	α_y	α_{xy}	α_x	α_{-yx}
1	+Z (South)	-3±2°	+2±2°	-1±2°	+0.5±2°
2	+Z	-3±2°	-1±2°	-2±2°	+0.5±2°
3	-Z (North)	-1±2°	-6±3°	-1±3°	-6±3°
4	-Z	-0.1±2°	-2±2°	+2±2°	+3±2°
	+Z	-1±2°	+1±2°	+0.5±2°	-3±2°
5	-Z	+1±1°	-1±5°	+1±1°	+2±1°
6	-Z	-2±2°	-0.3±2°	-0.3±2°	-1±2°
	+Z	-1±2°	+1±2°	+1±2°	+3±2°
Weighted Ave. North	-Z	0.5±0.8°	2±1°	0.7±0.9°	0.9±0.9°
Weighted Ave. South	+Z	2±0.9°	0.3±1°	0.2±0.9°	0.2±0.9°
Total Weighted Average		1±0.6°	0.7±0.7°	0.3±0.7°	0.5±0.6°

APPENDIX C

POSITRON BACKSCATTERING

The majority of positrons emitted do not directly enter a silicon detector, but rather strike the gold, aluminum, or sapphire of the bulb interior. A fraction of the positrons, which strike interior surfaces adjacent to detectors, backscatter into these detectors and produce counts that would not otherwise have been observed. If we define b as the backscattering contribution to the observed count rate N in a given detector, then

$$N = n + b \ ,$$

where n is the number that directly enter the detector without backscattering.

Because of the isotropy of positron emission with respect to the nuclear spin $\vec{I}$ (A in Eq. II-6 is 0.039) and the symmetry of the detector bulb assembly, b is assumed equal for all counters. Thus, in monitoring the polarization, if N is the observed rate for downstream EI counters, then the upstream rate will be

$$N' = n' + b \ .$$

The effect of backscattering is to reduce the measured polarization asymmetries Δ_A:

$$\Delta_A = \frac{N - N'}{N + N'} = \frac{n - n'}{n + n' + 2b} \approx \frac{n - n'}{n + n'}\left[1 - \frac{2b}{n + n'}\right] = \Delta_o S \ ,$$

where we have neglected background and counter efficiency differences and assumed that b is much less than either n or n'. The backscattering correction S is

$$S = \left(1 - \frac{2b}{n + n'}\right) \approx \left(1 - \frac{b}{n}\right)$$

for n ≈ n' and considering the "A" correlation in Eq. II-6:

$$\Delta_o = \frac{n - n'}{n + n'} = \mathrm{PGA}\,\frac{v}{c} \ .$$

Identical considerations hold for regular and image coincidence pairs used to measure the B and D asymmetries.

The ratio b/n of backscattered counts to "true" counts depends upon the bulb-detector geometry and the materials used. The walls of the converter boxes are Al and the insulators are glass with an average Z of 10. n and b can be defined as

$$n = N_o f_o \quad \text{and} \quad b = N_o f_1 \varepsilon f_2 \ ,$$

where N_o is the number of positrons emitted per unit time. The fraction of N_o that directly enters the detectors is f_o. The fraction that strike surfaces adjacent to detectors, from which positrons could backscatter into these same detectors, is f_1. ε is the backscattering coefficient (percentage of incident positrons that undergo backscattering), and f_2 is the percentage of backscattered positrons entering a given detector. Letting $f = f_1 \cdot f_2$, we have

$$S = (1 - \frac{f}{f_o}\varepsilon) \ .$$

For the geometry of the converter boxes and Si detectors used to monitor the polarization, $f \approx f_0$.

The value of ε for positrons is lower by a factor of 1.2 than that for electrons.[32] For the average-energy (1 MeV), normally-incident positron, $\varepsilon(\mathrm{Al}) \approx 0.10 \pm 0.01$.[33] This coefficient, for back-scattered positrons with energies above threshold, is $\varepsilon_T(\mathrm{Al}) \approx 0.05$.[34] For glancing incident scattering angles (~30° above surface), $\varepsilon_T(\mathrm{Al})$ can increase to 0.33.[34] The lower the Z, the greater this increase.

Assuming $\varepsilon(\mathrm{effective})_T \approx 0.15 \pm 0.1$, for approximately normal incidence we have $S = 0.85 \pm 0.1$. Since, for our particular geometry, a reasonable fraction of the backscattering is at near-grazing angles, our value of S probably represents an upper limit.

An evaluation of the backscattering contribution to the measured coincidence rates is extremely complicated, due to the intricate geometry of the bulb. Such an evaluation was not attempted. If, however, we assume that the major contribution to both positron and ion backscattering occurs due to grazing collisions on the walls of the converter boxes, the value of S obtained above can be used for the evaluation of the coefficient B in Sect. V. A more reliable evaluation of S is obtained in Sect. V using the known value of B and the present experimental data.

APPENDIX D

NUCLEAR SPIN RELAXATION DURING CONTAINMENT IN BULB

The successful observation of a possible T-odd angular correlation in the present experiment depends entirely upon the fact that nuclear spin relaxation mechanisms do not — despite ~10^5 wall collisions before escaping or decaying — substantially diminish the polarization of ^{19}Ne atoms. Estimates of the relaxation time T are made for several possible relaxation mechanisms. The results are given below for a 22-gauss field B_A. None of these adequately account for the observed average polarization P = 75 ± 5%, for a 4-sec sitting time, and P < 25% for a 10-sec sitting time.

	Perturbation		
	μ(Ne)·μ(Al)	μ(Ne)·μ(Bohr)	Field Inhomogeneities
Reflection	T=10^{12} sec	10^{10} sec	-
Adsorption	10^8 sec	10^6 sec	-
In Flight	-	-	10^3 sec

A. Relaxation During Collisions with Walls

Estimating the adsorption time of ^{19}Ne on the Teflon walls of a bulb, Dobson[27] calculated the relaxation times due to dipole-dipole interactions of μ_N(^{19}Ne) (nuclear) with (1) the fluorine in the Teflon and (2) paramagnetic molecules absorbed on the bulb walls, e.g., O_2. The bulb in this experiment is made of Al, Au, sapphire, and Pyrex, and is kept at a temperature of 200°K. For an adsorption time of approximately 10^{-11} sec, the relaxation times due to ^{19}Ne-^{27}Al and ^{19}Ne-Cr^{+++} dipole-dipole interactions are given in the above table. The most prevalent paramagnetic material in the bulb was not O_2, but the Cr^{+++} ions present as an impurity in sapphire at the 25-ppm level. Electrostatic quadrupole interactions cannot occur during collisions, since the quadrupole moment of neon is identically zero.

B. Relaxation In Flight

Magnetic field inhomogeneities encountered by the neon atoms as they move along random trajectories in the bulb may also cause spin relaxation. The results of Kleppner's analysis[36] of spin relaxation in the hydrogen maser may be applied to ^{19}Ne. To calculate T one must include the velocity distribution, the shape of the bulb, and a precise description of the inhomogeneities. If we assume inhomogeneities in the bulb given, in polar coordinates, by

$$\vec{B} = \left(B_A + \frac{B_T}{d^2(r^2 - 2z^2)}\right)\hat{z} + \frac{2B_T rz}{d^2}\,\hat{r} ,$$

where B_T is the magnitude of the inhomogeneities perpendicular to the z axes, and d is an effective bulb diameter, then we may use the expression

$$W = \frac{1}{4}\gamma^2(^{19}\mathrm{Ne})B_T^2 \frac{t_o}{1 + \left(\frac{\nu_L t_o}{2}\right)^4}$$

to estimate T. Here the gyromagnetic ratio is $\gamma = 2.9$ kHz/gauss, the Larmor frequency is $\nu_L = 57$ kHz, the transit time of the bulb is

$t_o \approx 10^{-4}$ sec, and the field inhomogeneity perpendicular to the z axis is $B_T \approx 10^{-2}$ gauss (we assume B_T is twice as large as that observed; see Sect. III). Using these values, T is 10^3 sec.

The relaxation times are orders of magnitude larger than the observed value of approximately 10 sec. This discrepancy indicates that the neon is sticking on and interacting with diffusion pump oil, or Si-based vacuum grease used to seal the bulb, or some unknown substance in the bulb. On the other hand, the number of collisions could be substantially larger than estimated. No effort was made to calculate this number using an exact model of the bulb and Monte Carlo methods.

APPENDIX E

GEOMETRY FACTORS

For each asymmetry Δ, the geometry factor G takes into account variations over the acceptable angles between $\hat{I}$, $\hat{p}$, and $\hat{r}$ which are possible with the finite decay volume and detector sizes, variations over all acceptable positron energies between $T_{\text{thresh}} = 0.5$ MeV/c and $T_{\text{max}} = 2.21$ MeV/c, and variations over the acceptable positron-ion time-delay intervals (0.27-3 μsec).

All geometry factors (and theoretical time-of-flight patterns) were calculated on the CDC 6600 computer using Monte Carlo methods. For G_B and G_D, 50,000 events were generated to obtain the results given below. An outline of the program used will be given. Within the -10-keV grid (see Fig. 15), a decay site is generated at random. A random position on the face of a positron detector is generated next and direction of the positron momentum $\hat{p}$ is thus fixed. With uniform probability between E_{thresh} and E_{max}, a positron energy is generated. Finally, a neutrino direction is generated. The direction and magnitude of the recoil-ion momentum $\vec{r}$ is then obtained from the conservation of energy and momentum.

For each event constructed in this way, an appropriate weight factor ($\delta\lambda$) is obtained from the rate equation $d\lambda$ (Eq. II-18), where $\hat{I}$ is chosen along the +z axes (+x axes) of Fig. 2 for the D (B) experiment. Only events for which the positron can actually enter the positron counter E1, without striking the bulb walls, were considered further (see Fig. 15a).

The direction of the recoil ion determines which ion detector, if any, is struck. The magnitude of the recoil momentum, $|\vec{r}|$, is used to determine the time of flight for the ion. In this way the T-O-F patterns are calculated. Since the total time of flight depends on where the ion strikes the sloped surface of the converter box foil, this triangular shape is included in the program.

The probability that two or more secondary electrons are produced for 10-keV ions, $\mathcal{P}(2)$, is obtained from an empirical formula obtained from secondary-electron-yield data.[30] Subject to a smaller potential difference, ions from events between grids (prompts — see Fig. 15b) have less energy and therefore a lower secondary-electron yield. (This was considered in the program.) The total weight factor is the product of $\delta\lambda$ and $\mathcal{P}(2)$, $n = \delta\lambda\mathcal{P}(2)$.

By generating events and recording the total weight factors for regular and image coincidence pairs in the way outlined above, the calculational method simulates the actual operation of the bulb. If, in calculating the weighting factors $\delta\lambda$ and $\delta\lambda'$ for the regular and image pairs in Table II, we set $D = 1$, $B = A = 0$ and neglect $\underline{a}$ in Eq. II-18, the expression for Δ_D is simply equal to the geometry factor. That is,

$$\Delta_D = \frac{n - n'}{n + n'} = G_D P + G_D ,$$

when P is set equal to one (1).

The results for a preset time delay interval of 0.27-3.0 μsec are

$$G_D^{135} = 0.42 \pm 0.03 \qquad G_D^{90} = 0.67 \pm 0.03 \qquad \text{(3.3 cm dia. inner grid.)}$$

$$G_D^{135} = 0.56 \pm 0.03 \qquad G_D = 0.77 \pm 0.04 \qquad \text{(2.5 cm dia. inner grid.)}$$

$$G_B^{1} = 0.48 \pm 0.03 \qquad G_B^{3} = 0.77 \pm 0.04 \qquad \text{(3.3 cm dia. inner grid.)}$$

where 5% errors are assigned.

The shape of the calculated time-of-flight (T-O-F) patterns obtained from this program agree quantitatively with the experimentally measured T-O-F patterns.

The calculation of G_A for the polarization measurement was considerably easier. Using another program, only randomly generated events which had a direct shot at the Si detectors were considered (see Fig. 15c). A random direction for positron emission was generated and only those events were accepted as hits for which the coordinates in the plane of the detector were within the sensitive volume of the Si detector. Including the region behind the detector,

$$G_A = 0.64.$$

(following page)

Fig. 15a. Schematic end view of bulb showing positron detection in E1. Light plus dark shading represents volume of bulb for which positrons can be observed by the positron counter shown. Light shading represents volume from which positrons as part of a coincidence event can be observed by E1. Acceleration of ions occurs between grids.

Fig. 15b. Schematic end view of bulb showing active volume inside -10-keV grid (light shading) from which ions can be detected in any ion counter. For each ion counter shown, dark shading indicates region between grids from which prompt ions, with energies less than 10 keV, can originate.

Fig. 15c. Side view of ion detector and converter box mounted on octagon. Shading both in front and behind Si detector indicates volume from which positrons contribute to the E1 singles rate used to monitor polarization.

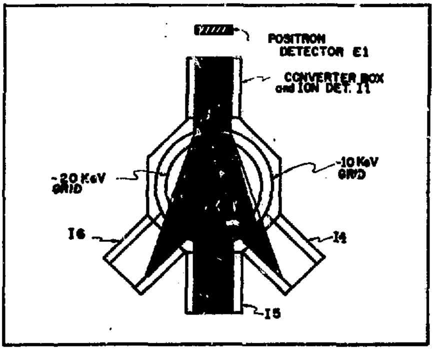

Fig. 15a

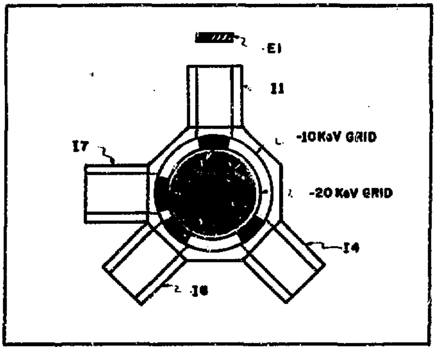

Fig. 15b

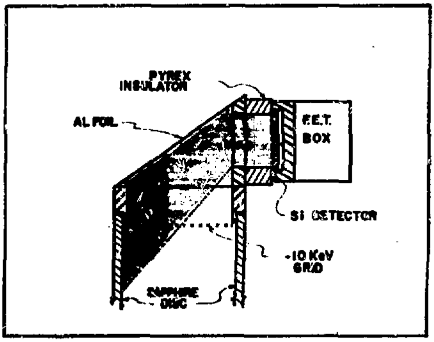

Fig. 15c

XBL 724-725

Fig. 15. *(see previous page)*

REFERENCES

1. F. P. Calaprice, E. D. Commins, H. M. Gibbs, G. L. Wick, and D. A. Dobson, Phys. Rev. 184, 1117 (1969); G. L. Wick (Ph.D. Thesis), Lawrence Radiation Laboratory Report No. UCRL-17708, 1967 (unpublished).
2. J. H. Christenson, J. W. Cronin, V. L. Fitch, and R. Turlay, Phys. Rev. Lett. 13, 138 (1964).
3. S. Bennett, D. Nygren, H. Saal, J. Steinberger, and J. Sunderland, Phys. Rev. Lett. 19, 993 (1967).
4. E. M. Henley, Parity and Time Reversal Invariance in Nuclear Physics, Ann. Rev. Nucl. Sci. 19, 367 (1969).
5. O. C. Kistner, Phys. Rev. Lett. 19, 872 (1967); M. Atac, B. Chrisman, P. Debrunner, and H. Frauenfelder, Phys. Rev. Lett. 20, 691 (1968); J. P. Hannon and G. T. Trammell, Phys. Rev. Lett. 21, 726 (1968); J. K. Baird, P. D. Miller, W. D. Dress, and N. F. Ramsey, Phys. Rev. 179, 1285 (1969).
6. C. S. Wu, The Conservation Laws in Beta Decay, in Alpha-, Beta-, and Gamma-Ray Spectroscopy, ed. Kai Siegbahn (North-Holland, Amsterdam, 1965), p. 1313.
7. J. A. Helland, M. J. Longo, and K. K. Young, Phys. Rev. Lett. 21, 257 (1968).
8. S. W. Barnes et al., Phys. Rev. 117, 238 (1960).
9. B. G. Erozolimski et al., Sov. J. Nucl. Phys. 11, 583 (1970).
10. K. K. Young, M. J. Longo, and J. A. Helland, Phys. Rev. Lett. 18, 806 (1967); Phys. Rev. 181, 1808 (1969).
11. O. E. Overseth and R. F. Roth, Phys. Rev. Lett. 19, 391 (1967).
12. S. Weinberg, Phys. Rev. 112, 1375 (1958).
13. R. E. Marshak, Riazuddin, and C. P. Ryan, Theory of Weak Interactions in Particle Physics (Wiley-Interscience, New York, 1969), p. 96.
14. Ibid., p. 107.
15. J. D. Jackson, S. B. Treiman, and H. W. Wyld, Jr., Phys. Rev. 106, 517 (1957).

16. J. D. Jackson, S. B. Treiman, and H. W. Wyld, Jr., Nucl. Phys. **4**, 206 (1957).

17. E. D. Commins and D. A. Dobson, Phys. Rev. Lett. **10**, 347 (1963).

18. B. R. Holstein, Phys. Rev. C **4**, 764 (1971).

19. M. L. Goldberger and K. M. Watson, *Collision Theory* (J. Wiley, New York, 1964), Chap. 9; J. Gillespie, *Final State Interactions* (Holden-Day, San Francisco, 1964).

20. J. J. Sakurai, *Invariance Principles and Elementary Particles* (Princeton Univ. Press, New York, 1964), p. 108; S. Gasiorowicz, *Elementary Particle Physics* (J. Wiley, New York, 1966), p. 515.

21. E. J. Konopinski, *The Theory of Beta Radioactivity* (Oxford Univ. Press, Oxford, 1966), p. 270.

22. J. B. Gerhart, Phys. Rev. **109**, 897 (1958).

23. H. Levtz and H. Wenninger, Nucl. Phys. **A99**, 55 (1967).

24. F. P. Calaprice, private communication, 1971; to be published in an article by B. R. Holstein.

25. C. G. Callan, Jr. and S. B. Treiman, Phys. Rev. **162**, 1494 (1967).

26. O. Koefoed-Hansen, Kgl. Danske Videnskab. Selskab, Mat.-Fys. Medd. **28**, 3 (1954).

27. D. A. Dobson (Ph.D. Thesis), Lawrence Radiation Laboratory Report No. UCRL-11169, 1963 (unpublished).

28. N. F. Ramsey, *Molecular Beams* (Oxford Univ. Press, Oxford, 1956), p. 399.

29. F. P. Calaprice (Ph.D. Thesis), Lawrence Radiation Laboratory Report No. UCRL-17551, 1967 (unpublished).

30. H. M. Gibbs and E. D. Commins, Rev. Sci. Instr. **37**, 1385 (1966).

31. B. R. Holstein, Phys. Rev. C **4**, 740 (1971); B. R. Holstein and S. B. Treiman, Phys. Rev. C **3**, 1921 (1971).

32. K.-D. Tillman, Energy Spectra of Backscattered Electrons and Positrons By Monte Carlo Calculations, 1970, Lawrence Radiation Laboratory Report No. UCRL-19719 (unpublished).

33. R. W. Dressel, Phys. Rev. **144**, 332 (1966).

34. D. H. Rester and J. H. Derrickson, Nucl. Instr. Meth. 86, 261 (1970).

35. S. Dushman, Scientific Foundations of Vacuum Technique (J. Wiley, New York, 1962).

36. D. Kleppner, H. Goldenberg, and N. F. Ramsey, Phys. Rev. 126, 603 (1962).

ACKNOWLEDGMENTS

I am delighted to express my special thanks to the following people who were instrumental in the success of this work:

Professor Eugene Commins for his advice, encouragement and direction as my thesis advisor, and for his help with the experiment and as a teacher throughout my graduate years.

Professor Frank Calaprice, my colleague and companion through those many months and late hours. His contributions, ideas, energy and sacrifices continuously made the difference.

Professor Howard Shugart for his interest and support during the entirety of this project, and particularly for his generous and timely help with the design and testing of the data handling system.

Mel Simmons for his energies and valuable contributions during many stages of this work.

Paul Goldsmith for his help with the study of the ion detectors.

I want also to acknowledge my indebtedness and personal thanks to all of those people who contributed to the progress and successful culmination of this work. Some of these are:

Dr. Bernard Harvey for his generous support and continuous backing at the 88-inch cycloton.

Fred Goulding and Don Landis and their staffs, who continuously contribute to so many experiments via electronic and detector design and support.

The entire crew of the 88-inch cyclotron for their cooperation, equipment, day-to-day help, and friendship. Special thanks must go to

Don Lundgren, Mat Renkas, Art Hartwig, and Harry Harrington.

Del Dietrich for his advice and superb craftsmanship in the fabrication of the bulb-detector system.

Doug MacDonald for engineering help and Warren Harnden for his fine work on the figures in this thesis.

Jean Atteridge, who organized the format and did the typing of this thesis.

My children Michael and Donna for their youthful and exuberant encouragement to finish.

My wife Eleanor for her patience and so much more during these years.

This work was supported by the U.S. Atomic Energy Commission.